Available online at www.sciencedirect.com

ScienceDirect

journal homepage: www.elsevier.com/locate/he

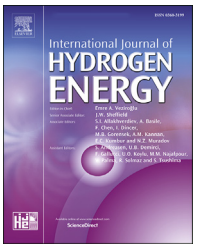

Large eddy simulation and finite-volume conditional moment closure modelling of a turbulent lifted H_2/N_2 flame

Guangze Li [a,b,c], *Huangwei Zhang* [c,*], *Longfei Chen* [a]

[a] *School of Energy and Power Engineering, Beihang University, Beijing 100191, China*
[b] *Beihang Hangzhou Innovation Institute Yuhang, Xixi Octagon City, Yuhang District, Hangzhou 310023, China*
[c] *Department of Mechanical Engineering, National University of Singapore, 9 Engineering Drive 1, Singapore 117576, Republic of Singapore*

HIGHLIGHTS

- Effects of the mesh resolution for the finite-volume CMC model are investigated.
- Effects of numerical schemes on convection term of CMC equation are assessed.
- Distributions of numerical fluxes on the CMC faces are presented.
- Budget analysis of the individual CMC terms in the CMC equation are conducted.

ARTICLE INFO

Article history:
Received 21 June 2021
Received in revised form
23 September 2021
Accepted 25 September 2021
Available online xxx

Keywords:
Lifted flame
Large eddy simulation
Conditional moment closure
Mesh resolution
Finite volume method

ABSTRACT

Large eddy simulations with three-dimensional finite-volume Conditional Moment Closure (CMC) model are performed for a hydrogen/nitrogen lifted flame with detailed chemical mechanism. The emphasis is laid on the influences of mesh resolution and convection scheme of finite-volume CMC equations on predictions of reactive scalars and unsteady flame dynamics. The results show that the lift-off height is underestimated and the reactive scalars are over-predicted with coarser CMC mesh. It is also found that further refinement of the CMC mesh would not considerably improve the results. The time sequences of the most reactive and stoichiometric hydroxyl radical mass fractions indicate that finer CMC mesh can capture more unsteady details than the coarser CMC mesh. Moreover, the coarse CMC mesh has lower conditional scalar dissipation rate, which would promote the earlier auto-ignition of the flame base. Besides, the effects of the convection scheme for the CMC equations (i.e., upwind, central differencing and their blends) on the lifted flame characteristics are also investigated. It is shown that different convection schemes lead to limited differences on the time-averaged temperature, mixture fraction and species mass fractions. Moreover, the root-mean square values of hydrogen and hydroxyl mass fractions show larger deviation from the measurements with hybrid upwind and central differencing scheme, especially around the flame base. Furthermore, the distributions of the numerical fluxes on the CMC faces also show obvious distinctions between the upwind and blending schemes. The budget analysis of the individual CMC terms shows that a sequence of CMC faces has comparable contributions with upwind scheme. However, with the hybrid schemes, the instantaneous flux is dominantly from limited CMC

* *Corresponding author.*
E-mail address: huangwei.zhang@nus.edu.sg (H. Zhang).
https://doi.org/10.1016/j.ijhydene.2021.09.209

Please cite this article as: Li G et al., Large eddy simulation and finite-volume conditional moment closure modelling of a turbulent lifted H_2/N_2 flame, International Journal of Hydrogen Energy, https://doi.org/10.1016/j.ijhydene.2021.09.209

faces. The reactivity of a CMC cell is more easily to be affected by its neighbors when the upwind scheme is used.

Introduction

Turbulent lifted flames have been extensively adopted in practical combustion apparatus, including industrial burner and propulsion system, since they can prevent the nozzle from being damaged by the high-temperature zone [1–5]. Meanwhile, the fuel and oxidant can achieve a certain level of pre-mixing through diffusion and turbulent motion ahead of the flame base. It is generally accepted that lift-off, blow-off and stabilization of the flame are affected by the mutual interaction of turbulence and chemical kinetics [6]. Clear understanding of the complex mechanism behind the lifted flame is of great importance to design and improve the industrial combustion devices.

Numerous experimental studies on turbulent lifted flames have been performed [7–13]. For instance, Cabra et al. [7] designed a vitiated co-flow burner to explore the features of lifted turbulent H_2/N_2 (hydrogen/nitrogen) jet flames, and they measured the temperature and key species concentrations in the lifted flame. Using the same burner as in Ref. [7], Wu et al. [8] investigated the correlation between the lift-off height and various flow conditions (e.g. jet/co-flow velocities and co-flow temperature). Their results reveal that the lift-off height increases with jet/co-flow velocities and decreases with co-flow temperature. Moreover, Markides and Mastorakos [9] experimentally studied the autoignition behaviors of hydrogen in a co-flowing air, and they reported the similar correlations between the flame lift-off height and co-flow velocity/temperature to those by Wu et al. [8] In addition, Leung and Wierzba [10] further studied the co-flow velocity effects on stability of turbulent non-premixed jet flame and they found that the co-flow velocity considerably influences the blowout limits of the lifted flames.

Due to the simple flow configurations and well-defined boundary conditions, turbulent lifted flames are widely used for combustion model validations [14,15]. The Conditional Moment Closure (CMC) approach has been shown to be able to accurately predict the turbulent lifted flames [16–24]. For instance, the Large eddy Simulation – Conditional Moment Closure (LES-CMC) approach was used to simulate a lifted methane flame by Navarro-Martinez et al. [22], and their results show that the flow characteristics and reactive scalars are predicted well by the LES-CMC model. The effects of the inflow turbulence on lift-off height were also captured satisfactorily. They used the same model to investigate various lifted hydrogen flames [21], i.e. Berkeley experiments [7] and Cambridge experiments [9], which further corroborate the prediction accuracy of the sub-grid scale CMC model. Moreover, Stankovic [20] simulated hydrogen auto-ignition in a turbulent co-flow of heated air also with LES-CMC approach, and various experimentally observed autoignition regimes are reproduced by LES-CMC. With LES-CMC, Tyliszczak [23] assessed the effects of different models of conditional scalar dissipation rate on auto-ignition of lifted hydrogen flame, and it is shown that the predicted lift-off height is sensitive to the model constant for sub-grid scale scalar dissipation. Rosiak and Tyliszczak [24] studied the flame development and propagation of a pure hydrogen jet in a hot co-flow of oxygen and water vapor with LES-CMC approach, and found that the changes of the oxidizer composition can affect the flame temperature and lift-off height.

In the above LES-CMC simulations [16–24], the CMC equations are discretized with finite differencing method on a different mesh from the LES one. Recently, to achieve higher prediction accuracy of the physical transport term discretization and accommodate more realistic turbulent flame problems (e.g. model gas turbine combustors), the LES-CMC model based on finite volume discretization is implemented, extended from the previous Cambridge finite-differencing solver [25–27]. The essence of this implementation is to discretize the CMC equations (more specifically physical transport terms and relevant quantities) based on the surface fluxes through the CMC cell faces and these CMC faces are automatically selected from the cell faces of fine LES mesh. The improvements for the CMC simulations include: 1) Polyhedral CMC cells can be used, rendering it suitable for complicated flame configurations (e.g. model burners and/or variable inlet conditions). This is an important step for an advanced combustion model for real applications. 2) Since the CMC faces are selected from the LES faces, the numerical fluxes are essentially resolved at the (fine) LES resolution, instead of the (coarse) CMC resolutions. Therefore, the variations (e.g. fluctuations) of the surface fluxes for a CMC cell can be accurately captured, compared to the numerical discretization done over the coarse CMC resolutions. 3) At the inlet conditions, due to the surface flux calculations based on LES (or CMC) faces, the inlet condition effects (e.g. inlet turbulence) on the near-inlet CMC cells are accurately quantified. It has been validated in predicting localized/global extinctions and forced ignition in turbulent non-premixed flames [25,28–31]. However, whether the finite volume CMC model can accurately predict the auto-ignition of turbulent lifted flames has not been examined yet. Clarifying this would be helpful to extend the finite volume CMC model for more complicated problems, e.g. turbulent lifted spray flames.

Moreover, despite the successful applications of the finite-volume CMC model [25,26,28–31], the sensitivity to the model implementations has not been particularly investigated. It is known that due to distinct LES and CMC meshes, the CMC resolution may affect the calculations of reactive scalars in mixture fraction space and strong spatial variation of flame structure in physical space. Stankovic et al. [19] used LES with the finite differencing CMC to investigate the Cabra lifted H_2/N_2 flame [7], and they found that the refinement of CMC mesh may move the flame base further downstream. Navarro-

Please cite this article as: Li G et al., Large eddy simulation and finite-volume conditional moment closure modelling of a turbulent lifted H_2/N_2 flame, International Journal of Hydrogen Energy, https://doi.org/10.1016/j.ijhydene.2021.09.209

Martinez and Kronenburg also analyzed various CMC resolutions in their LES of different lifted flames with one- and two-dimensional CMC models [21], and observed that the coarser CMC mesh would produce an unrealistically flat temperature profile at the flame base. Therefore, whether the conclusions from the above work [19,21] can be straightforwardly extended to the three-dimensional finite volume CMC model is uncertain. Besides, the interactions between the neighboring CMC cells (characterized by the convection and sub-grid scale diffusion of the conditional reactive scalars) have significant effects on capturing highly unsteady and localized flame dynamics (e.g. localized extinction, blow-off and re-ignition) [21,28]. In Refs. [25,26,28–31], the upwind scheme is used for the convection term in the CMC equations. With it, the transport direction of conditional reactive scalars in physical space is dominantly controlled by the local mass or volume flux. Whether the dissipative nature of this scheme affects the predictions of instantaneous and/or local flame dynamics needs to be assessed. It is worth mentioning that both the numerical schemes and the ratios of CMC and LES filter sizes are numerical parameters that may influence the prediction accuracies of the LES-CMC model.

In this work, the effects of CMC resolution and numerical scheme will be studied. The lifted H_2/N_2 flame [7] is selected as the target flame. The reasons include: 1), The uncertainties of hydrogen chemical mechanism are relatively small; 2), There are plenty of experimental data measured for model validations; 3), The richness of unsteady flame dynamics, such as flame autoignition and stabilization as well as turbulence-chemistry interaction, is helpful for examining the prediction ability of the LES-CMC model. In this work, three CMC meshes are adopted to investigate the CMC resolution sensitivity in the framework of finite volume discretization. It is worth mentioning that the finest CMC mesh studied in this work is identical to the LES mesh, which is helpful to assess the accuracies of the data exchange between the LES and CMC meshes. Furthermore, three convection schemes, including upwind scheme, hybrid upwind and central differencing schemes with different blending factors, are employed to explore the discretization scheme effects.

The rest of the manuscript is structured as below. Section Governing equation presents the governing equations for LES and CMC modelling. The flame information and numerical implementation are introduced in Section Flame information and numerical implementation, followed by the results and discussion in Section Results and discussion. The main conclusions are summarized in Section Conclusion.

Governing equation

Large eddy simulation

In LES, the large-scale eddies are resolved, while the effects of the unresolved small-scale eddies on the resolved flow field are modelled. Their governing equations can be derived through low-pass filtering the respective instantaneous equations. In this work, the resolved continuity and momentum equations are solved [32].

$$\frac{\partial \overline{\rho}}{\partial t}+\frac{\partial \overline{\rho}\tilde{u}_i}{\partial x_i}=0, \tag{1}$$

$$\frac{\partial \overline{\rho}\tilde{u}_i}{\partial t}+\frac{\partial \overline{\rho}\tilde{u}_i\tilde{u}_j}{\partial x_j}=-\frac{\partial \overline{p}}{\partial x_i}+\frac{\partial \tilde{\tau}_{ij}}{\partial x_j}-\frac{\partial \tau_{ij}^{sgs}}{\partial x_j}, \tag{2}$$

where t is time, x is spatial coordinate, $\overline{\rho}$ is resolved density, $\overline{p}$ is resolved pressure and $\tilde{u}$ is resolved velocity. $\tilde{\tau}_{ij}=\mu\left(\frac{\partial \tilde{u}_i}{\partial x_j}+\frac{\partial \tilde{u}_j}{\partial x_i}-\frac{2}{3}\frac{\partial \tilde{u}_k}{\partial x_k}\delta_{ij}\right)$ is resolved stress tensor with δ_{ij} being Kronecker delta function. μ is dynamic viscosity, which is estimated based on Sutherland's law. $\tau_{ij}^{sgs}=\overline{\rho}(\widetilde{u_iu_j}-\tilde{u}_i\tilde{u}_j)$ is the sub-grid scale stress tensor, closed by the constant Smagorinsky model [33].

For modelling turbulent non-premixed flames, the resolved mixture fraction $\tilde{\xi}$ is solved from

$$\frac{\partial \overline{\rho}\tilde{\xi}}{\partial t}+\frac{\partial \overline{\rho}\tilde{\xi}\tilde{u}_j}{\partial x_j}=\frac{\partial}{\partial x_j}\left[\overline{\rho}D\frac{\partial \tilde{\xi}}{\partial x_j}+\overline{\rho}\left(\widetilde{\xi u_j}-\tilde{\xi}\tilde{u}_j\right)\right], \tag{3}$$

where D refers to the molecular mass diffusion coefficient. With the unity Lewis number assumption, D is calculated through the thermal conductivity as $D=k/\rho C_p$. For turbulent flames, generally, the molecular diffusion is less important due to the strong turbulent transport. Therefore, the Lewis number was assumed to be unity in this work, which is one of the intrinsic assumptions of the CMC model. The assumption has been relaxed in some previous CMC studies [34,35], and it has been shown that the results with and without this assumption are similar. Here k is the thermal conductivity, calculated using the Eucken approximation [26], i.e. $k=\mu C_v(1.32+1.37R/C_v)$. Here C_v is the heat capacity at constant volume and derived from $C_v=C_p-R$. Here $C_p=\sum_{m=1}^{M}Y_mC_{p,m}$ is the heat capacity at constant pressure, and $C_{p,m}$ is estimated from JANAF polynomials [27]. A gradient-type model is adopted to estimate the sub-grid scalar flux in Eq. (3), i.e.

$$\overline{\rho}\left(\widetilde{\xi u_j}-\tilde{\xi}\tilde{u}_j\right)=-\overline{\rho}D_t\frac{\partial \tilde{\xi}}{\partial x_j}, \tag{4}$$

Here $D_t=\mu_t/\overline{\rho}Sc_t$ is sub-grid scale diffusivity with μ_t being sub-grid scale dynamic viscosity. The Sc_t is turbulent Schmidt number and is assumed as 0.7 [36].

The sub-grid mixture fraction variance $\tilde{\xi''^2}$ is calculated by an algebraic model [37]

$$\tilde{\xi''^2}=c_v\Delta^2\frac{\partial \tilde{\xi}}{\partial x_i}\frac{\partial \tilde{\xi}}{\partial x_i}, \tag{5}$$

Δ is the LES filter width and is taken as the cube root of the LES cell volume, i.e., $\Delta=V_{LES}^{1/3}$. V_{LES} is the volume of a LES cell. The constant c_v in Eq. (5) is assumed to be 0.1 [37]. Moreover, the scalar dissipation rate $\tilde{N}$ includes the contributions from the resolved mixture fraction field (i.e. $\tilde{N}_{res}$) and the sub-grid one (i.e. $\tilde{N}_{sgs}$) [38]

$$\tilde{N}=\tilde{N}_{res}+\tilde{N}_{sgs}=\underbrace{\frac{\partial \tilde{\xi}}{\partial x_i}\frac{\partial \tilde{\xi}}{\partial x_i}D}_{resolved}+\underbrace{\frac{c_N}{2}\frac{\mu_t}{\overline{\rho}\Delta^2}\tilde{\xi''^2}}_{sub-grid} \tag{6}$$

Please cite this article as: Li G et al., Large eddy simulation and finite-volume conditional moment closure modelling of a turbulent lifted H_2/N_2 flame, International Journal of Hydrogen Energy, https://doi.org/10.1016/j.ijhydene.2021.09.209

The sub-grid scale scalar dissipation rate $\tilde{N}_{sgs}$ is modelled based on the assumption that a characteristic velocity time-scale is proportional to a characteristic mixing time scale [38–40], which is parameterized by the model constant c_N in Eq. (6). This constant characterizes the contribution of scalar dissipation from the sub-grid field on the total one, i.e. $\tilde{N}$. Tyliszczak [23] performed a systematic analysis on the sensitivity of CMC modelling of the Cabra flame to this constant [7] and the results suggested that the lift-off height can be accurately reproduced when $c_N = 120$, which is followed in our LES – CMC simulations.

Conditional moment closure model

The governing equation for the conditionally filtered species mass fraction can be written as [40–42]

$$\frac{\partial Q_\alpha}{\partial t}+\widetilde{u_k|\eta}\frac{\partial Q_\alpha}{\partial x_k}=\widetilde{N|\eta}\frac{\partial^2 Q_\alpha}{\partial \eta^2}+\widetilde{\omega_\alpha|\eta} -\frac{1}{\widetilde{\rho|\eta}\tilde{P}(\eta)}\frac{\partial}{\partial x_k}[\widetilde{\rho|\eta}\tilde{P}(\eta)(u_k\widetilde{Y_\alpha|\eta}-\widetilde{u_k|\eta}Q_\alpha)], \tag{7}$$

where $Q_\alpha \equiv \widetilde{Y|\eta}$ is the conditional filtered mass fraction of α-th species. η is the sample space variable for mixture fraction, whereas the operator "$(\cdot|\eta)$" means conditioning on mixture fraction. $\widetilde{u_k|\eta}$, $\widetilde{N|\eta}$ and $\widetilde{\omega_\alpha|\eta}$ are the conditional filtered velocity, scalar dissipation rate and reaction rate of α-th species, respectively. The filtered density function $\tilde{P}(\eta)$ is assumed to be β-shaped and calculated with the filtered mixture fraction $\tilde{\xi}$ and its variance $\tilde{\xi''^2}$. $\widetilde{\rho|\eta}$ is conditionally filtered density. Note that the CMC equation is practically solved on a different grid resolution Δ_{CMC} from the LES one Δ_{LES} and normally the former is coarser than the latter [42–44]. Therefore, the LES and CMC equations are filtered with various filter sizes.

The second term on the LHS can be divided into two terms

$$\widetilde{u_k|\eta}\frac{\partial Q_\alpha}{\partial x_k}=\frac{\partial}{\partial x_k}(\widetilde{u_k|\eta}Q_\alpha)-Q_\alpha\frac{\partial \widetilde{u_k|\eta}}{\partial x_k}. \tag{8}$$

The last term on the RHS of Eq. (7) can be modelled with a gradient-type model [44]

$$u_k\widetilde{Y_\alpha|\eta}-\widetilde{u_k|\eta}Q_\alpha=-D_t\frac{\partial Q_\alpha}{\partial x_k}. \tag{9}$$

Neglecting $\widetilde{\rho|\eta}\tilde{P}(\eta)$ and substituting Eqs. (8) and (9) into Eq. (7), one can obtain the following governing equation for Q_α

$$\frac{\partial Q_\alpha}{\partial t}+\frac{\partial}{\partial x_k}(\widetilde{u_k|\eta}Q_\alpha)=Q_\alpha\frac{\partial \widetilde{u_k|\eta}}{\partial x_k}+\widetilde{N|\eta}\frac{\partial^2 Q_\alpha}{\partial \eta^2}+\widetilde{\omega_\alpha|\eta}+\frac{\partial}{\partial x_k}\left(D_t\frac{\partial Q_\alpha}{\partial x_k}\right). \tag{10}$$

The product of conditional density and filtered density function in the last term (sub-grid diffusion) in the RHS of Eq. (7) is moved out of the spatial derivative and therefore cancelled out, resulting in its form in Eq. (10). This simplification is based on the following reasons: (1) when the value of $\tilde{P}(\eta)$ equals zero, the last term in Eq. (7) numerically tends to be infinity, and this may increase the calculation uncertainties; (2) the diffusion flux through one CMC cell is actually summed from all the LES faces constituting that CMC cell in our implementation (see Section Finite volume discretization of CMC equations), and the LES mesh resolution is sufficiently small to make sense of neglecting the gradient of $\widetilde{\rho|\eta}\tilde{P}(\eta)$ across these faces. This has been used in our previous work [25,30,31] and reasonable predictions of the reactive statistics in mixture fraction space and physical space are achieved.

Integrating the above governing equation within a control volume Ω^{CMC} yields

$$\underbrace{\int_{\Omega^{CMC}}\frac{\partial Q_\alpha}{\partial t}d\Omega}_{T_0}+\underbrace{\int_{\Omega^{CMC}}\frac{\partial Q_\alpha}{\partial x_k}(\widetilde{u_k|\eta}\,Q_\alpha)d\Omega}_{T_1}=\underbrace{\int_{\Omega^{CMC}}Q_\alpha\frac{\partial \widetilde{u_k|\eta}}{\partial x_k}d\Omega}_{T_2} +\underbrace{\int_{\Omega^{CMC}}\widetilde{N|\eta}\frac{\partial^2 Q_\alpha}{\partial^2 \eta}d\Omega}_{T_3}+\underbrace{\int_{\Omega^{CMC}}\widetilde{\omega_\alpha|\eta}d\Omega}_{T_4}+\underbrace{\int_{\Omega^{CMC}}\frac{\partial}{\partial x_k}\left(D_t\frac{\partial Q_\alpha}{\partial x_k}\right)d\Omega}_{T_5}, \tag{11}$$

where Ω^{CMC} represents the CMC cell. The first term in the LHS, T_0, is unsteady term, whilst the terms T_1 and T_2 denote conditional convection and dilatation, respectively. T_3 represents micro-mixing, T_4 chemical reaction, and T_5 sub-grid scale conditional scalar flux. In our work, the conditionally filtered total enthalpy $Q_h \equiv \widetilde{h|\eta}$ is solved from

$$\int_{\Omega^{CMC}}\frac{\partial Q_h}{\partial t}d\Omega+\int_{\Omega^{CMC}}\frac{\partial}{\partial x_k}(\widetilde{u_k|\eta}\,Q_h)d\Omega=\int_{\Omega^{CMC}}Q_\alpha\frac{\partial \widetilde{u_k|\eta}}{\partial x_k}d\Omega +\int_{\Omega^{CMC}}\widetilde{N|\eta}\frac{\partial^2 Q_h}{\partial^2 \eta}d\Omega+\int_{\Omega^{CMC}}\frac{\partial}{\partial x_k}\left(D_t\frac{\partial Q_h}{\partial x_k}\right)d\Omega, \tag{12}$$

which is similar to Eq. (11) without chemical reaction term T_4.

The Amplitude Mapping Closure (AMC) model [45] is employed to model $\widetilde{N|\eta}$ in the LES resolution, i.e.,

$$\widetilde{N|\eta}=N_0G(\eta), \tag{13}$$

$$N_0=\tilde{N}\Big/\int_0^1\tilde{P}(\eta)G(\eta)d\eta, \tag{14}$$

$$G(\eta)=exp\left(-2\left[erf^{-1}(2\eta-1)\right]^2\right). \tag{15}$$

Here $G(\eta)$ is a shape function and calculated from the inverse error function $erf^{-1}(x)$. The conditionally filtered scalar dissipation rate in CMC cells (denoted with superscript "CMC") and they are calculated by integrating $\widetilde{N|\eta}$ over all the LES cells within one CMC cell [40]

$$\widetilde{N|\eta}^{CMC}=\frac{\int_{\Omega^{CMC}}\overline{\rho}\tilde{P}(\eta)\widetilde{N|\eta}d\Omega}{\int_{\Omega^{CMC}}\overline{\rho}\tilde{P}(\eta)d\Omega}. \tag{16}$$

The mixture fraction and its variance on a CMC cell, $\tilde{\xi}^{CMC}$ and $\tilde{\xi''^2}^{CMC}$, are given as [40].

Please cite this article as: Li G et al., Large eddy simulation and finite-volume conditional moment closure modelling of a turbulent lifted H_2/N_2 flame, International Journal of Hydrogen Energy, https://doi.org/10.1016/j.ijhydene.2021.09.209

$$\tilde{\xi}^{CMC} = \frac{\int_{\Omega^{CMC}} \overline{\rho}\tilde{\xi} d\Omega}{\int_{\Omega^{CMC}} \overline{\rho} d\Omega}, \tag{17}$$

$$\tilde{\xi''^2}^{CMC} = \frac{\int_{\Omega^{CMC}} \overline{\rho}\tilde{\xi''^2} d\Omega}{\int_{\Omega^{CMC}} \overline{\rho} d\Omega} + \frac{\int_{\Omega^{CMC}} \overline{\rho}\tilde{\xi}^2 d\Omega}{\int_{\Omega^{CMC}} \overline{\rho} d\Omega} - \left(\frac{\int_{\Omega^{CMC}} \overline{\rho}\tilde{\xi} d\Omega}{\int_{\Omega^{CMC}} \overline{\rho} d\Omega}\right)^2 \tag{18}$$

First-order CMC model is used in this work and hence the conditionally filtered reaction rate can be modelled as $\widetilde{\omega_\alpha|\eta} \approx \omega_\alpha(Q_1, \ldots Q_n, Q_T)$. Here n represents the total number of species, and $Q_T \equiv \widetilde{T|\eta}$ is the conditionally filtered temperature. Finally, the unconditionally filtered variables $\tilde{f}$ (e.g., $\overline{\rho}$, $\tilde{T}$ and $\tilde{Y}_\alpha$) are obtained by integrating the conditional value $\widetilde{f|\eta}$ in mixture fraction space

$$\tilde{f} = \int_0^1 \widetilde{f|\eta}\tilde{P}(\eta) d\eta, \tag{19}$$

in which $\widetilde{f|\eta}$ is the conditionally filtered scalars (e.g., $1/\widetilde{\rho|\eta}$, Q_T and Q_α).

Finite volume discretization of CMC equations

For the current LES – CMC formulations, the mesh for CMC equation discretization, Ω^{CMC}, is reconstructed from the LES cells, which is shown in Fig. 1. The CMC nodes (red dots in Fig. 1) are generated within the same domain as that for LES. Then the centroids of the LES cells (i.e. blue dots) search for the host CMC node based on the minimal distance algorithms, i.e. the distance between the centroid of the LES cell and its host CMC node is the smallest. With this, the LES cells have, and only have, unique CMC nodes. Furthermore, the CMC faces (dashed lines in Fig. 1) are selected from the LES faces such that the host CMC nodes of the LES cells sharing them are different. The individual CMC nodes can be enclosed by a sequence of CMC faces. The polyhedral CMC control volumes are therefore generated, and the CMC governing equations, Eqs. (11) and (12), are discretized over them. The finite volume discretization of the individual terms in Eq. (11) are detailed as below.

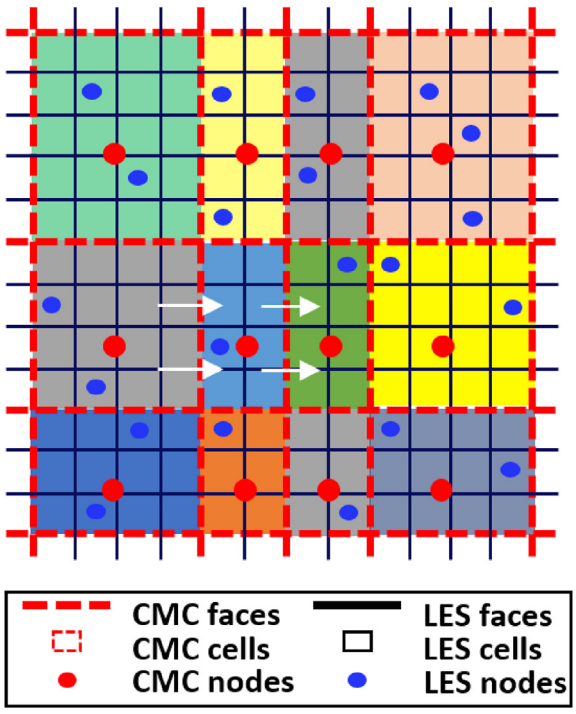

Fig. 1 – Schematic of CMC cell reconstruction from LES mesh. The arrows indicate the directions of convective fluxes of Q_α or Q_h. Each LES cell and CMC cell has individual nodes.

- Term T_0 (unsteadiness)

$$\int_{\Omega^{CMC}} \frac{\partial Q_\alpha}{\partial t} d\Omega \approx \frac{\partial}{\partial t}\int_{\Omega^{CMC}} Q_\alpha d\Omega \approx V^{CMC}\frac{\partial Q_\alpha}{\partial t}, \tag{20}$$

where V^{CMC} is the volume of a CMC cell.

- Term T_1 (convection)

$$\int_{\Omega^{CMC}} \frac{\partial}{\partial x_k}(\widetilde{u_k|\eta}Q_\alpha) d\Omega = \oint_{\partial\Omega^{CMC}} (\widetilde{u_k|\eta}Q_\alpha) \cdot \mathbf{n} dS, \tag{21}$$

$\partial\Omega^{CMC}$ refers to the faces of a CMC cell.

$$\oint_{\partial\Omega^{CMC}} (\widetilde{u_k|\eta}Q_\alpha) \cdot \mathbf{n} dS = \sum_{m=1}^{F^{CMC}} \oint_{\partial\Omega^{CMC}} (\widetilde{u_k|\eta}Q_\alpha \cdot \mathbf{n}) \Delta S_m = \sum_{m=1}^{F^{CMC}} (\widetilde{u_x|\eta}Q_\alpha n_x + \widetilde{u_y|\eta}Q_\alpha n_y + \widetilde{u_z|\eta}Q_\alpha n_z)_m \Delta S_m, \tag{22}$$

in which F^{CMC} stands for the number of LES faces surrounding the CMC node. The quantities, n_x, n_y and n_z, are the Cartesian components of the CMC face normal vectors. $\widetilde{u_x|\eta}$, $\widetilde{u_y|\eta}$ and $\widetilde{u_z|\eta}$ are the Cartesian components of $\widetilde{u|\eta}$. The convection fluxes

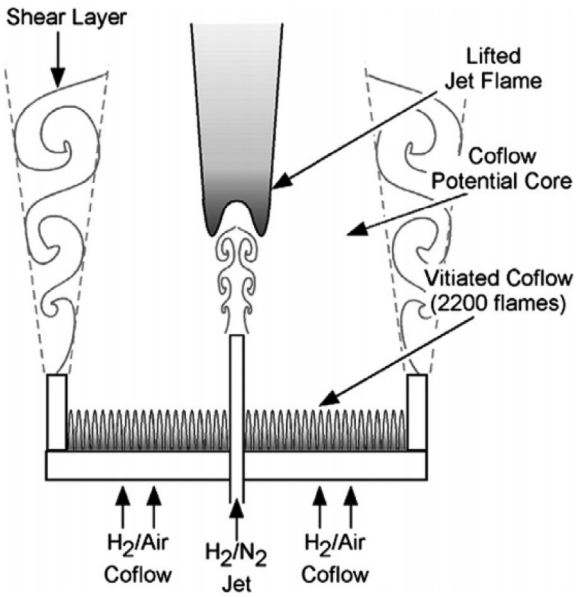

Fig. 2 – Schematic of the Berkeley H_2/N_2 flame [7].

Please cite this article as: Li G et al., Large eddy simulation and finite-volume conditional moment closure modelling of a turbulent lifted H_2/N_2 flame, International Journal of Hydrogen Energy, https://doi.org/10.1016/j.ijhydene.2021.09.209

are expected to influence the physical transport between the neighboring CMC cells, indicated by the arrows as showed in Fig. 1. One can see from Eqs. (21) and (22) that the species flux from one CMC cell would be gained by the neighboring one and therefore it is conserved.

As mentioned before, $\widetilde{u_k|\eta}$ is modelled as $\tilde{u}_k$ [42], Eq. (22) can be re-written as

$$\sum_{m=1}^{F^{CMC}}\left(\widetilde{u_x|\eta}Q_\alpha n_x+\widetilde{u_y|\eta}Q_\alpha n_y+\widetilde{u_z|\eta}Q_\alpha n_z\right)_m\Delta S_m=\sum_{m=1}^{F^{CMC}}\left(\tilde{u}_xQ_\alpha n_x+\tilde{u}_yQ_\alpha n_y+\tilde{u}_zQ_\alpha n_z\right)_m\Delta S_m \tag{23}$$

The effects of numerical schemes for convection term T_1 will be studied in this work, including Upwind (UD) scheme and blended UD/CD (Central Differencing) schemes [46].

The blended scheme of CD and UD is implemented with a blending factor γ

$$\phi_m=\gamma(\phi_m)_{CD}+(1-\gamma)(\phi_m)_{UD}, \tag{24}$$

where ϕ_m is a generic variable ϕ (e.g. $\widetilde{u_k|\eta}Q_\alpha$) at the m-th face. $(\phi_m)_{CD}$ and $(\phi_m)_{UD}$ are the numerical fluxes predicted with CD and UD schemes, respectively. γ is a tuneable parameter, and $\gamma=1$ denotes CD scheme, whereas $\gamma=0$ denotes UD scheme.

- Term T_2 (dilatation)

$$\int_{\Omega^{CMC}}Q_\alpha\frac{\partial\widetilde{u_k|\eta}}{\partial x_k}d\Omega=Q_\alpha\int_{\Omega^{CMC}}\frac{\partial\widetilde{u_k|\eta}}{\partial x_k}d\Omega=Q_\alpha\oint_{\partial\Omega^{CMC}}\widetilde{u_k|\eta}\cdot ndS, \tag{25}$$

where we assumed that Q_α is constant within a CMC cell [40,42]. Since $\widetilde{u_k|\eta}$ is modelled as $\tilde{u}_k$ [42], Eq. (25) can be re-written as

$$\oint_{\partial\Omega^{CMC}}\widetilde{u_k|\eta}\cdot ndS\approx\oint_{\partial\Omega^{CMC}}\tilde{u}_k\cdot ndS\approx\sum_{m=1}^{F^{CMC}}\left(\tilde{u}_xn_x+\tilde{u}_yn_y+\tilde{u}_zn_z\right)_m\Delta S_m, \tag{26}$$

where $\tilde{u}_x$, $\tilde{u}_y$ and $\tilde{u}_z$ are the Cartesian components of filtered velocity $\tilde{u}$ at the m-th LES faces, respectively.

- Term T_3 (micro-mixing)

$$\int_{\Omega^{CMC}}\widetilde{N|\eta}\frac{\partial^2Q_\alpha}{\partial^2\eta}d\Omega\approx V^{CMC}\widetilde{N|\eta}\frac{\partial^2Q_\alpha}{\partial\eta^2} \tag{27}$$

Here both $\widetilde{N|\eta}$ and $\frac{\partial^2Q_\alpha}{\partial\eta^2}$ are assumed to be constant in one CMC cell.

- Term T_4 (chemistry)

$$\int_{\Omega^{CMC}}\widetilde{\omega_\alpha|\eta}d\Omega\approx V^{CMC}\widetilde{\omega_\alpha|\eta}. \tag{28}$$

It is assumed that the reaction rate $\widetilde{\omega_\alpha|\eta}$ does not change within one CMC cell and therefore can be moved out of the integration over the CMC cell.

- Term T_5 (sub-grid scale diffusion)

$$\int_{\Omega^{CMC}}\frac{\partial}{\partial x_k}(D_t\nabla Q_\alpha)d\Omega=\oint_{\partial\Omega^{CMC}}(D_t\nabla Q_\alpha)\cdot nS=\sum_{m=1}^{F^{CMC}}D_{t,m}\left(\frac{\partial Q_\alpha}{\partial x}n_x+\frac{\partial Q_\alpha}{\partial y}n_y+\frac{\partial Q_\alpha}{\partial z}n_z\right)_m\Delta S_m, \tag{29}$$

where $D_{t,m}$ is the sub-grid diffusivity at the m-th CMC face. The derivatives, $\partial Q_\alpha/\partial x$, and $\partial Q_\alpha/\partial y$, are the Cartesian components of the gradient of $\partial Q_\alpha/\partial z$. The discretization of the individual CMC terms in Eq. (12) are the same and therefore not repeated here.

Flame information and numerical implementation

Berkeley H_2/N_2 flame

The lifted H_2/N_2 flame in a vitiated co-flowing jet measured by Cabra et al. [7] is simulated in this work. The schematic of this burner is shown in Fig. 4. The central jet of H_2 and N_2 is injected from a burner with a diameter of $D_j=4.57$ mm. A vitiated co-flow of the combustion products from a lean pre-mixed H_2/air flame is provided to ignite the central fuel jet. The conditions of the central jet and surrounding co-flow are listed in Table 1. The central jet consists of 25% H_2 and 75Q_α% N_2 (by volume), while the vitiated co-flow is 14.74% O_2 (oxygen), 75.34% N_2 and 9.89% H_2O (water). The temperatures of the fuel and co-flow are 305 K and 1045 K, respectively. The bulk velocity of the fuel jet is $U_j=107$ m/s, while the co-flow velocity is 3.5 m/s. Their Reynold numbers are 23,600 and 18,600, respectively. Furthermore, the stoichiometric mixture fraction ξ_{st} is 0.474, calculated based on Bilger's formulation [47]. There exists a most reactive mixture fraction around which autoignition occurs first due to optimal thermo-chemical conditions [48] and it is about 0.054 for this flame. The measured lift-off height of this flame is about $10D_j$ [7].

Numerical implementation

A cylindrical domain is used for LES and CMC simulations. It starts from the burner exit plane, and the domain size in the axial, radial and azimuthal directions are $30D_j\times10D_j\times2\pi$, respectively. The coordinate origin lies at the center of the H_2/N_2 fuel jet. Different CMC resolutions will be studied in this work, which will be detailed in Section Simulation case.

Table 1 – Boundary conditions at fuel jet and co-flow.

Parameters	Fuel jet	Co-flow
Diameter	4.57 mm (D_j)	210 mm
Temperature	305 K	1045 K
Velocity	107 m/s (U_j)	3.5 m/s
Mole fraction of H_2	0.25	0
Mole fraction of O_2	0	0.1474
Mole fraction of N_2	0.75	0.7534
Mole fraction of H_2O	0	0.0989
Reynold number	23,600	18,600

Please cite this article as: Li G et al., Large eddy simulation and finite-volume conditional moment closure modelling of a turbulent lifted H_2/N_2 flame, International Journal of Hydrogen Energy, https://doi.org/10.1016/j.ijhydene.2021.09.209

Besides, mixture fraction space is discretized by 51 nodes with two boundaries at $\eta = 0$ (co-flow) and $\eta = 1$ (fuel jet), respectively, and the nodes are clustered around the stoichiometric and most reactive mixture fractions.

In the LES, for the fuel jet, one-seventh power law is applied for the mean axial velocity of the fuel jet, consistent with the experiments [7]. The synthetic eddy method [49] is used to reproduce the turbulence and the Reynolds stress components are estimated following Masri et al. [50] Top-hat profile is given for the co-flow mean velocity. The mixture fraction is unity at the jet, while zero at the co-flow. Zero-gradient condition is enforced for all the quantities at the lateral and outlet boundaries.

For the CMC boundaries in the physical space, mixing solutions of Q_α and Q_h are specified at both fuel jet and co-flow. The thermo-chemical compositions at the two boundaries, i.e. $\eta = 0$ and $\eta = 1$, follow the conditions of fuel jet and co-flow tabulated in Table 1. Zero-gradient condition for Q_α and Q_h is applied at the lateral and outlet boundaries. The CMC cells in the interior domain are initialized by the mixing solutions.

The LES governing equations, i.e. Eqs. (1)–(3), are solved with OpenFOAM®, whilst the CMC equations (Eqs. (11) and (12)) are solved by an in-house CMC solver developed at University of Cambridge [25,26,29,31]. The two solvers are interfaced through on-the-fly data exchange (e.g. filtered density and temperature) at each time step, following the strategies detailed in Refs. [25,26,29,31]. The PIMPLE algorithm[†] is adopted for the coupling between velocity and pressure in LES, and first-order implicit Euler scheme is used for time discretization. Both convection and diffusion terms in the LES equations are discretized by central differencing scheme. For the CMC equations, the second-order central differencing is used for sub-grid diffusion term, whereas the linear interpolation is applied for dilatation term. The micro-mixing term in Eqs. (11) and (12) is calculated with TDMA (Tridiagonal Matrix Algorithm) method, and the ODE solver VODPK [51] is used for the chemical reaction terms $\widetilde{\omega_\alpha|\eta}$. Different schemes for convection term in the CMC equations will be studied, and the detailed information is presented in Section Simulation case. A chemical mechanism of 10 species and 23 reactions is used for hydrogen oxidation [52], which is also used in Refs. [53,54] for modelling the same flame. The time step for both LES and CMC solvers is 10^{-6} s. 48 bi-processors 2.60 GHz cores are used from ASPIRE 1 Cluster from National Supercomputing Center in Singapore. The Flow-Through Time (FTT) of this flame is $T_j = L_x/U_j \approx 1.3\ ms$, where L_x is the streamwise length of the computational domain. The statistical results in Section Results and discussion are collected over 10 FTT after the initial field effects are purged (over 10 FTT).

Simulation case

In this work, the LES mesh is 134 × 54 × 42 hexahedral cells and its sufficiency in resolving the flow kinetic energy and conserved scalar mixing can be confirmed by a mesh sensitivity and turbulence length scale estimations in Appendices A–C. To explore the CMC resolution effects, three CMC meshes are studied in Cases 1 – 3, respectively. Their detailed information is summarized in Table 2. The base (intermediate) CMC mesh in Case 1 contains 94 × 36 × 24 cells, whilst the fine CMC mesh in Case 2 has 134 × 54 × 42 and the coarse one in Case 3 consists of 54 × 36 × 24 cells. They are differentiated with CMC resolutions in the flame region, i.e. $10D_j \times 1.5D_j \times 2\pi$. The approximated ratios of the LES cells to CMC cells in Cases 1–3 are 4, 1 and 8, respectively. Note that in Case 2 the CMC mesh is the same as that of the LES mesh. Meanwhile, three convection schemes are considered, including UD and blended UD/CD schemes. These are compared through Cases 1, 4 and 5, as tabulated in Table 2.

Results and discussion

Basic flame structure

Fig. 3 shows the resolved profiles of temperature and OH (hydroxyl) mass fraction of Case 1 when the flame stabilizes. It is found that when $x/D_j < 10$, there is no obvious increase of temperature and OH mass fraction, indicating chemical reactions are week there. Nevertheless, when $x/D_j \geq 10$, high temperature and OH mass fractions are observable. This implies that the flame has ignited and been lifted beyond a critical height. Based on Fig. 3, the instantaneous lift-off height is around $10D_j$. This is determined from the minimal axial distance where the OH mass fraction reaches 2×10^{-4} [55,56]. Almost the same lift-off heights are obtained if other criteria (e.g. $\tilde{T} > 1800$ K) are used. Our results indicate that the flame base fluctuates between $8.7D_j$ and $11.5D_j$, similar to the experimental observations [57]. Similar fluctuations ($3 - 4D_j$) of the lift-off height are also reported by the previous LES – CMC simulations [21]. A closer inspection of Fig. 3 reveals that the OH radical is largely presented closer to the isolines of ξ_{mr} at the base. This indicates that the flame is stabilized with local auto-ignition around $10D_j$.

The time-averaged temperature and OH mass fraction from Case 1 are plotted in Fig. 4. It is seen that the mean lift-off height is about $10D_j$, which is consistent with the measurement in the experiment [7]. Note that this height is predicted without tuning the co-flow temperature or velocity, considering their possible uncertainties [7,8]. In the previous LES of the same flame with finite-differencing CMC model, the pronounced deviations (with the errors of $\pm 5D_j$) are observed for the lift-off height [20,21]. The mean temperature rises near the

Table 2 – Information on the simulation cases.

Case	Numerical scheme	CMC mesh	LES cell number per CMC cell
1 (base)	Blended scheme ($\gamma = 0.7$)	94 × 36 × 24	4
2	Blended scheme ($\gamma = 0.7$)	134 × 54 × 42	1
3	Blended scheme ($\gamma = 0.7$)	54 × 36 × 24	8
4	Blended scheme ($\gamma = 0.5$)	94 × 36 × 24	4
5	Upwind scheme	94 × 36 × 24	4

[†] In OpenFOAM®, PIMPLE algorithm is a combination of PISO (Pressure Implicit with Splitting of Operator) and SIMPLE (Semi-Implicit Method for Pressure-Linked Equations) methods.

Please cite this article as: Li G et al., Large eddy simulation and finite-volume conditional moment closure modelling of a turbulent lifted H_2/N_2 flame, International Journal of Hydrogen Energy, https://doi.org/10.1016/j.ijhydene.2021.09.209

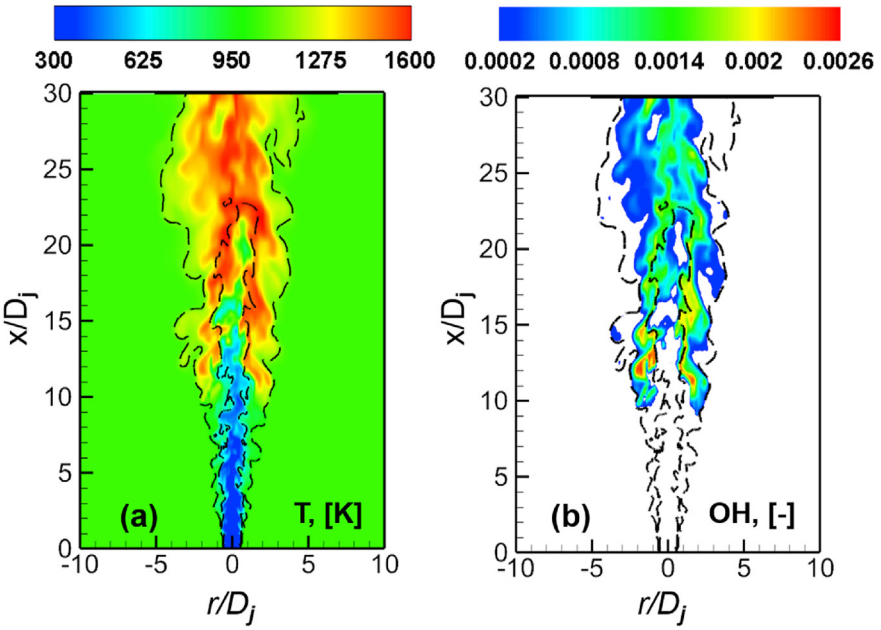

Fig. 3 – Resolved (a) temperature and (b) OH mass fraction. The inner isolines correspond to the stoichiometric mixture fraction ($\xi_{st} = 0.474$), while the outer isolines the most reactive mixture fraction ($\xi_{mr} = 0.054$).

fuel-lean mixture conditions, which is also seen from the resolved temperature in Fig. 3a. The mean OH mass fraction increases since the lift-off height. It peaks between $12D_j$ and $17D_j$ and at the fuel-lean side of the stoichiometric mixture fraction isolines.

Effects of CMC resolution

Three CMC meshes (i.e. Cases 1–3) are used to study the CMC resolution effects. Cases 1–3 respectively correspond to intermediate (base), fine and coarse resolutions, as listed in Table 2. Fig. 5 shows the radial profiles of mean temperature at six locations in Cases 1, 2 and 3. At $x/D_j = 1$, 14 and 26, the radial profiles of the mean temperature in Cases 1, 2 and 3 are in good accordance with the experimental data. However, the mean temperature from coarse CMC mesh, i.e. Case 3, are evidently over-predicted at the axial locations $x/D_j = 8$, 10 and 11. For instance, the mean temperature between $r/D_j < 2$ at $x/D_j = 10$ is higher than the experimental data, indicating that the auto-ignition phenomena have occurred there. This

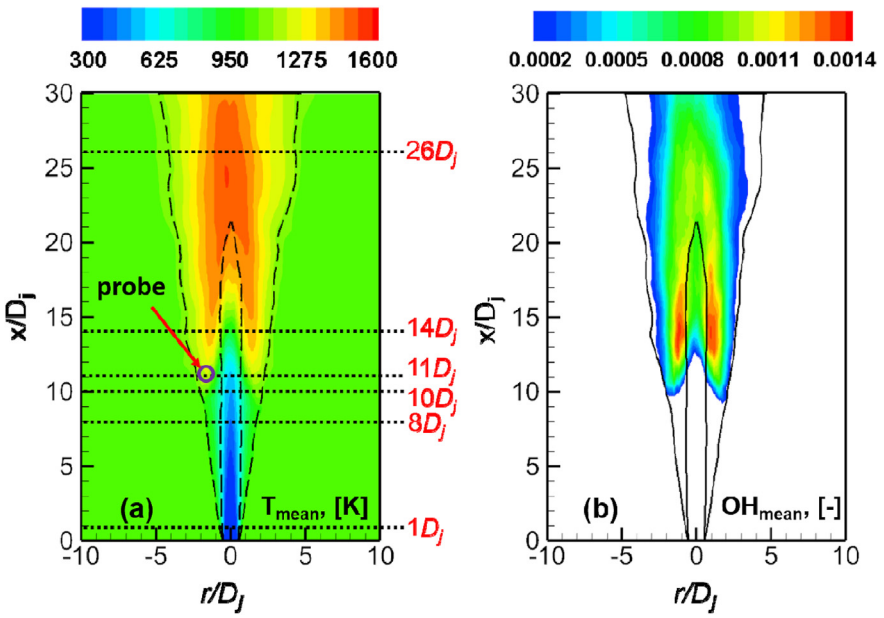

Fig. 4 – Time-averaged (a) temperature and (b) OH mass fraction. Legend for iso-lines same as in Fig. 2. Probe coordinate: $x = 11D_j$, $y = 1.4D_j$, $z = 0$.

Please cite this article as: Li G et al., Large eddy simulation and finite-volume conditional moment closure modelling of a turbulent lifted H_2/N_2 flame, International Journal of Hydrogen Energy, https://doi.org/10.1016/j.ijhydene.2021.09.209

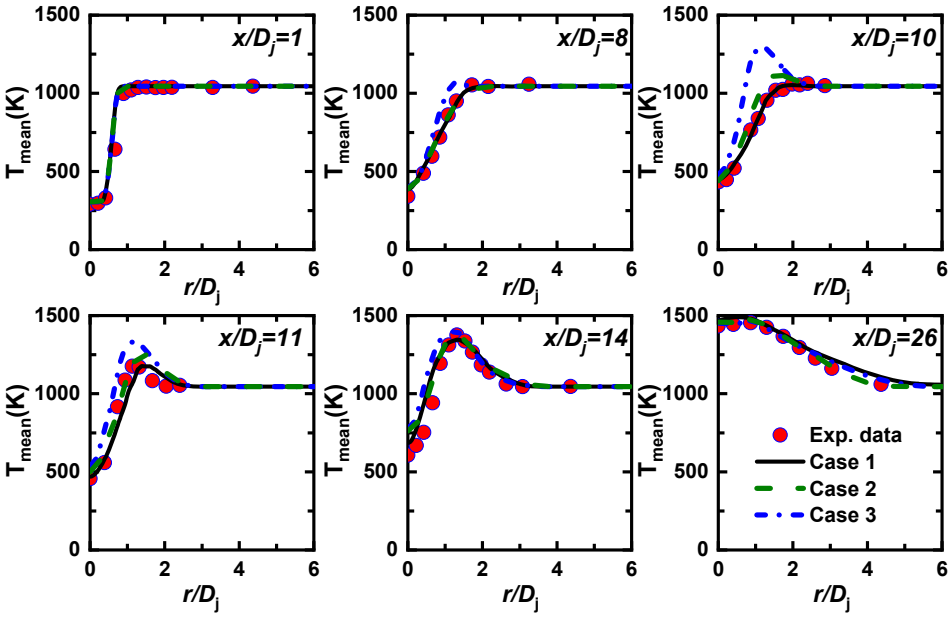

Fig. 5 – Radial profiles of time-averaged temperature at six axial locations. Experimental data from Ref. [7].

implies that the flame base stabilizes more upstream when the coarse CMC mesh is used, which results in lower lift-off height (about $7.7D_j$) in Case 3. Additionally, the radial profiles of the mean temperatures predicted with medium and fine CMC meshes (i.e. Cases 1 and 2) almost have no differences at $x/D_j = 8$, 10 and 11. This corroborates the accuracy in predicting the unsteady flame dynamics when non-consistent LES and CMC resolutions are used [40,42].

Fig. 6 shows the radial distributions of the temperature Root-Mean-Square (RMS) value at four locations, i.e. $x/D_j = 8$, 10, 11 and 14. Here the RMS values are calculated based on the resolved temperature. It is seen that the trends of the radial profiles of the temperature RMS at four axial locations are well captured with in Cases 1–3. The predictions of the coarse CMC mesh in Case 3 show largest deviations from the measurements than the other two at $x/D_j = 8$ and 10. However, at $x/D_j = 11$ and 14, the differences of the temperature RMS are relatively small, although the computed temperature RMS slightly deviates from the measured data.

The radial profiles of the statistics of H_2 and OH mass fractions at four axial locations are presented in Figs. 7 and 8, respectively. In Fig. 7, the mean H_2 mass fractions in Cases 1 and 2 are basically consistent with the measurements, while hydrogen consumption in Case 3 is slightly overestimated at $x/D_j = 10$, which is associated with the lower lift-off height predicted with the coarse mesh. The radial distributions of the RMS values of H_2 mass fraction show some deviations from the measurements, particularly at $x/D_j = 10$ and 11. The OH radical is an important indicator for the beginning of the hydrogen auto-ignition [9]. The predictions with the coarse CMC mesh suggest that the flame is initiated at around $7.7D_j$. Furthermore, the predicted mean and RMS of the OH mass fractions from the coarse CMC mesh are noticeably larger than the measurements at $x/D_j = 8$, 10 and 11. Differences of the mean OH mass fractions between the measurements and Cases 1 and 2 are small compared with those in the coarse mesh.

Multiple Mapping Conditioning (MMC) is a theoretically rigorous combination of Probability Density Functions (PDF) [58] and CMC models incorporating a generalisation of mapping closure [59,60]. The concepts of generalised MMC and sparse-Lagrangian LES are combined to form the sparse-Lagrangian LES-MMC model by Sundaram et al. [61]. For the

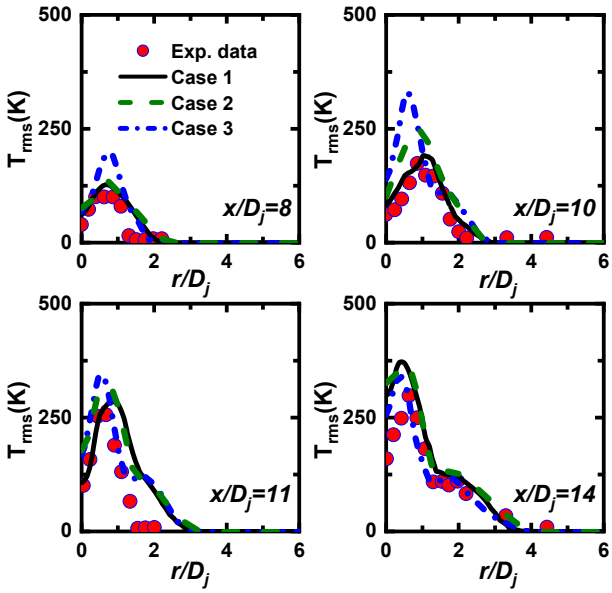

Fig. 6 – Radial profiles of temperature RMS at four axial locations. Experimental data from Ref. [7].

Please cite this article as: Li G et al., Large eddy simulation and finite-volume conditional moment closure modelling of a turbulent lifted H_2/N_2 flame, International Journal of Hydrogen Energy, https://doi.org/10.1016/j.ijhydene.2021.09.209

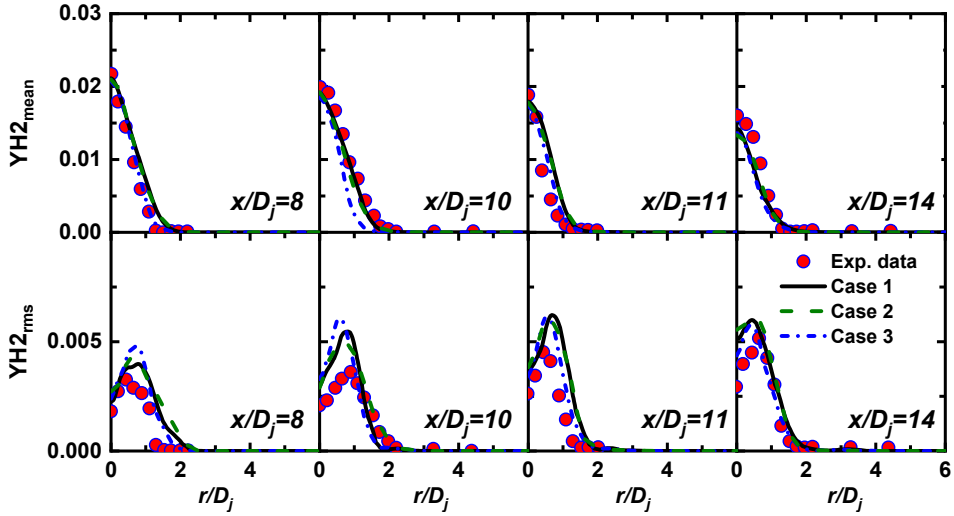

Fig. 7 – Radial profiles of mean (first row) and RMS (second row) of H_2 mass fraction at four axial locations. Experimental data from Ref. [7].

LES-MMC model, the fields of velocity, pressure and reference mixture fraction are obtained with an Eulerian LES, and the reactive composition field is obtained with a Lagrangian formulation of the Filtered Density Function (FDF) and the MMC method. The comparison between the axial profiles of temperature statistics predicted from LES-MMC [61] and this work (Case 1) are illustrated in Fig. 9. It can be found that the current LES-CMC model has the comparable accuracies with the LES-MMC model. The computational cost of the current LES-CMC simulation is slightly more expensive than that with the sparse-Lagrangian MMC method [61] (private communication, M. Cleary), but good parallelization efficiency of our CMC solver significantly reduces the computational cost, which makes the LES simulations affordable. It has to acknowledge that there are many additional effects influencing the computational costs besides the combustion model, including numerical solver, mesh and computational infrastructure.

The influences of CMC mesh resolution on conditionally filtered mass fraction are shown in Fig. 10. Here conditionally filtered OH mass fractions at stoichiometry ($\widetilde{Y_{OH}|\xi_{st}}$) is selected, as OH is an important indicator of auto-ignition event. Demonstration of $\widetilde{Y_{OH}|\xi_{st}}$ in the LES mesh is equivalent to visualizing that in the CMC resolution, since each LES cell in its host CMC cell has the same solutions. It can be found from Fig. 10 that the instantaneous distributions of $\widetilde{Y_{OH}|\xi_{st}}$ around the flame base look similar in Cases 1 and 2, while that

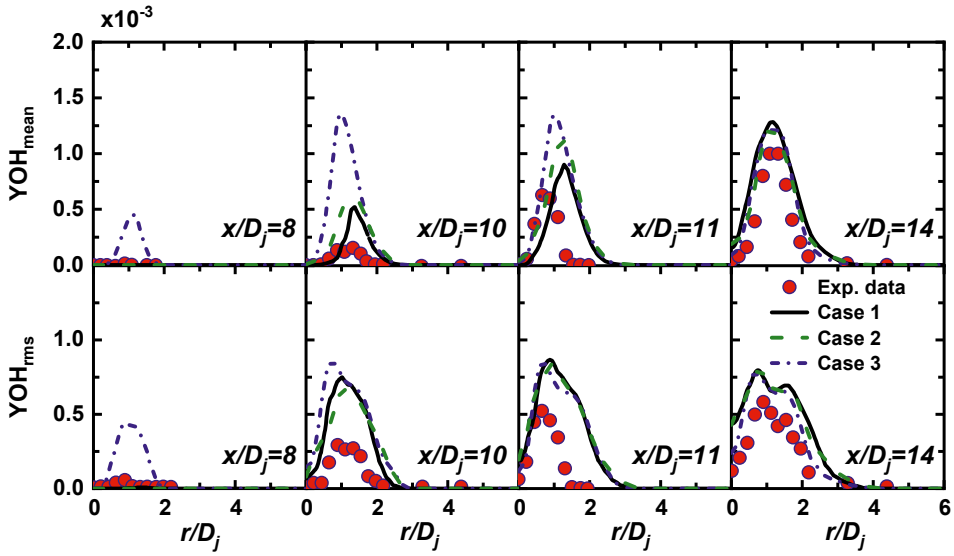

Fig. 8 – Radial profiles of mean (first row) and RMS (second row) of OH mass fraction at four axial locations. Experimental data from Ref. [7].

Please cite this article as: Li G et al., Large eddy simulation and finite-volume conditional moment closure modelling of a turbulent lifted H_2/N_2 flame, International Journal of Hydrogen Energy, https://doi.org/10.1016/j.ijhydene.2021.09.209

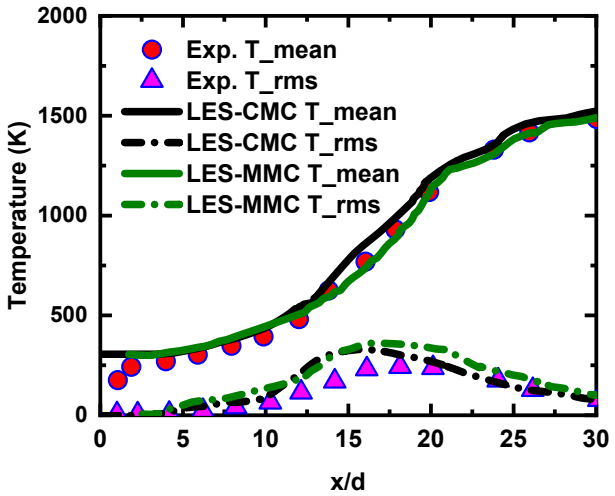

Fig. 9 – Comparison between the axial temperature statistics predicted with LES-MMC [55] and LES-CMC models.

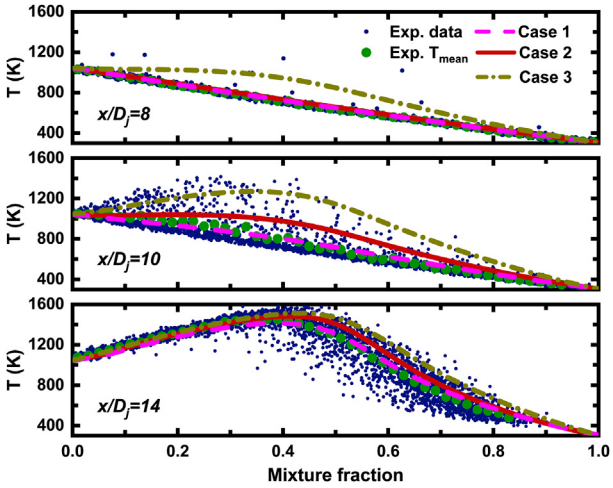

Fig. 11 – Scatter and conditional mean of temperature at three axial locations. Experimental data from Ref. [7].

from Case 3 is obviously different. Specifically, the flame base in Case 3 is lower than those in the other two, and meanwhile the gradient of $\widetilde{Y_{OH}|\xi_{st}}$ at the flame base is smaller than those in Cases 1 and 2.

To quantitatively analyze the effects of the CMC mesh resolution on the conditional flame structures, the scatter data from the experiments [7] and the conditional mean temperature at three axial locations (x/D_j = 8, 10 and 14) are illustrated in Fig. 11. The scatter data, including temperature and OH mass fraction, are collected from r/D_j = 0.066 to 1.88 along the radial direction at the abovementioned axial locations, and the simulation results are also extracted from the same locations. At $x/D_j = 8$, the conditional mean temperature in Cases 1 and 2 shows good accordance with the measurements, while those in Case 3 are over-predicted. At x/D_j = 10, near the flame base, differences between the measured and calculated conditional mean temperature in Cases 1 and 2 are small. The temperature scatters at x/D_j = 10 show that the mixing solutions are dominant at this location, although there are some points away from the mixing line. The latter corresponds to the possible instantaneous localized extinction and re-ignition near the flame base. Over-predictions of the conditional mean temperature in Case 3 at the three locations indicate that higher reactivity (earlier autoignition) at these locations due to the coarse CMC mesh used.

Fig. 12 shows the temperature fluctuations with respect to the conditional mean values in Cases 1–3 at the same axial locations as in Fig. 11. It can be found that the predicted temperature fluctuations of Case 2 are consistent with the measured values. This may be because the same LES and CMC mesh is used, which removes the need for data transfer between two meshes and leads to high resolution for conditional reactive scalars (e.g. temperature). Moreover, the results from Case 1 are closer to the experimental data than those from Case 3 at the three locations. Generally, increasing CMC mesh

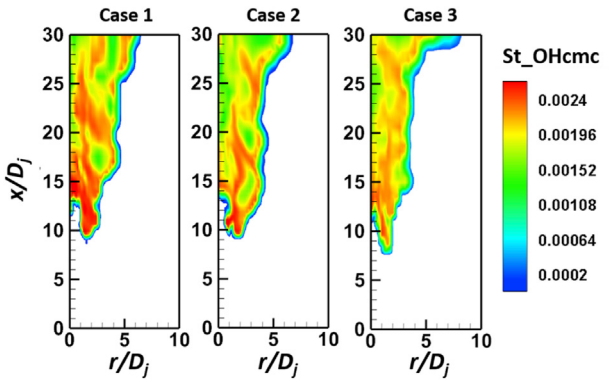

Fig. 10 – Contours of instantaneous conditionally filtered OH mass fractions at stoichiometry from different CMC meshes.

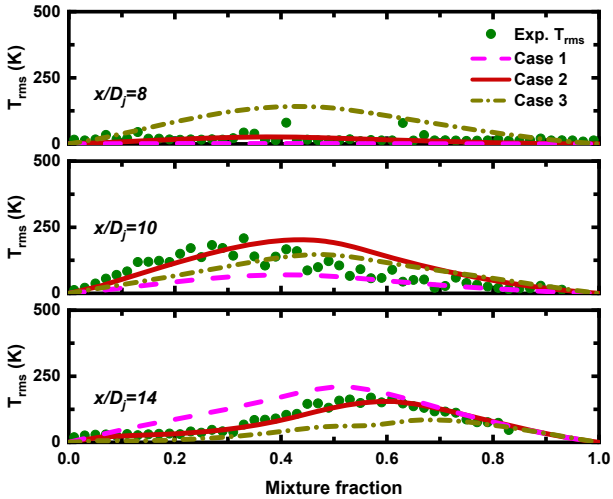

Fig. 12 – Conditional temperature fluctuation at three axial locations. Experimental data from Ref. [7].

Please cite this article as: Li G et al., Large eddy simulation and finite-volume conditional moment closure modelling of a turbulent lifted H_2/N_2 flame, International Journal of Hydrogen Energy, https://doi.org/10.1016/j.ijhydene.2021.09.209

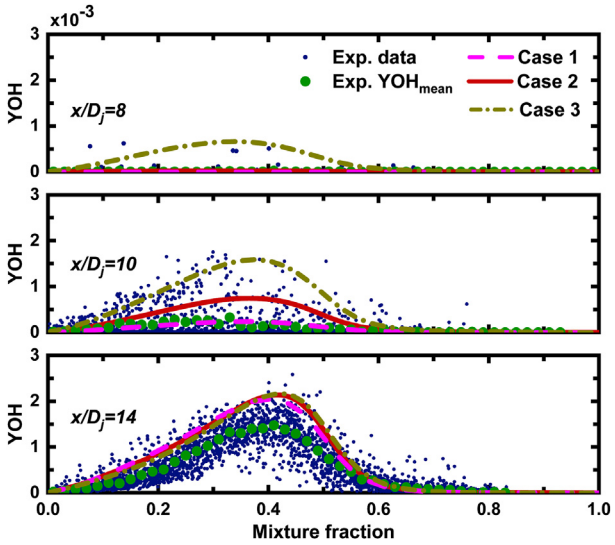

Fig. 13 – Conditional mean OH mass fraction at three axial locations. Experimental data from Ref. [7].

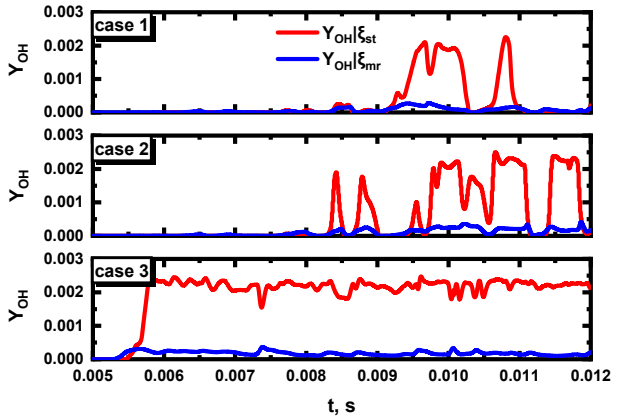

Fig. 15 – Time history of the most reactive and the stoichiometric OH mass fraction. Results from the probe ($x/D_j = 11$, $y/D_j = 1.4$, $z/D_j = 0$) shown in Fig. 2(a).

resolution enhances the accuracy of the LES – CMC model in capturing the unsteady temperature evolutions.

The conditional means and fluctuations of OH mass fraction at the same three locations are demonstrated in Figs. 13 and 14, respectively. It is apparent from Figs. 13 and 14 that the conditional mean OH mass fractions are sensitive to the CMC mesh resolution. The deviations of the OH mass fractions between the measurements and the predictions of Cases 1 and 2 are small compared with those of Case 3, similar to the tendency in Fig. 11. This is consistent with the comparison of the unconditional OH mass fraction in Fig. 8. Similar to the temperature fluctuations in Fig. 12, the fluctuations of conditionally mean OH mass fraction of Case 2 show better agreements with the measurements comparing with Cases 1 and 3.

Fig. 15 shows the time evolutions of OH mass fractions at most reactive (ξ_{mr}) and stoichiometric (ξ_{st}) mixture fractions. They are extracted from the probed CMC cell ($x/D_j = 11$, $y/D_j = 1.4$, $z/D_j = 0$, marked in Fig. 4a) in Cases 1–3. It can be found that this cell in Case 3 first achieves fully burning state at around 0.0058 s, while in Cases 1 and 2 ignition in the same location is initiated around 0.0085 s and 0.008 s, respectively. The phenomenon is in accordance with the flame solution in physical space as shown in Fig. 8, attributed to the fact that the flame lift-off height calculated from the coarse CMC mesh (Case 3) is lower than that from the refiner meshes (Cases 1 and 2). Meanwhile, more remarkable fluctuations of OH mass fractions at both mixture fractions are captured in Cases 1 and 2 compared with Case 3, as the finer CMC mesh can capture more details of turbulence. It is also seen from Cases 1 and 2 that the variations of the most reactive OH mass fraction are basically consistent with the variations of the stoichiometric OH mass fraction. However, this tendency is not clear in Case 3, although some small variations are also present.

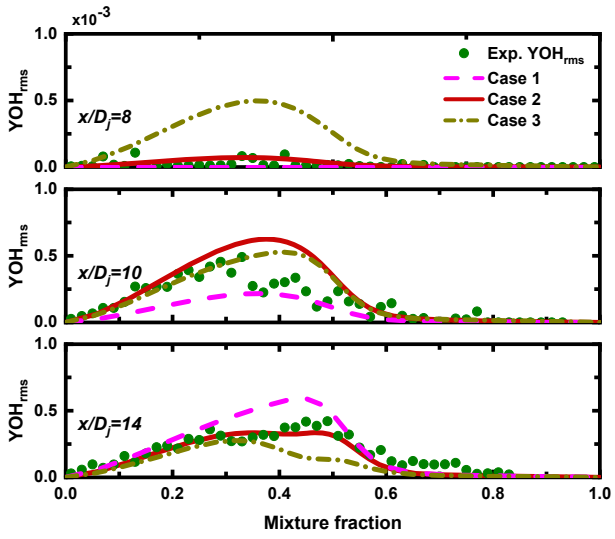

Fig. 14 – Conditional fluctuation of OH mass fraction at three axial locations. Experimental data from Ref. [7].

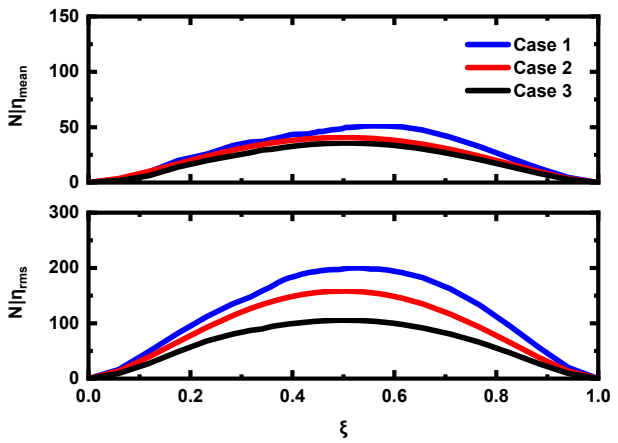

Fig. 16 – Mean and RMS of conditional scalar dissipation rate ($\widetilde{N|\eta}^{CMC}$) in mixture fraction space. Results from the probe ($x/D_j = 11$, $y/D_j = 1.4$, $z/D_j = 0$) shown in Fig. 2(a).

Please cite this article as: Li G et al., Large eddy simulation and finite-volume conditional moment closure modelling of a turbulent lifted H_2/N_2 flame, International Journal of Hydrogen Energy, https://doi.org/10.1016/j.ijhydene.2021.09.209

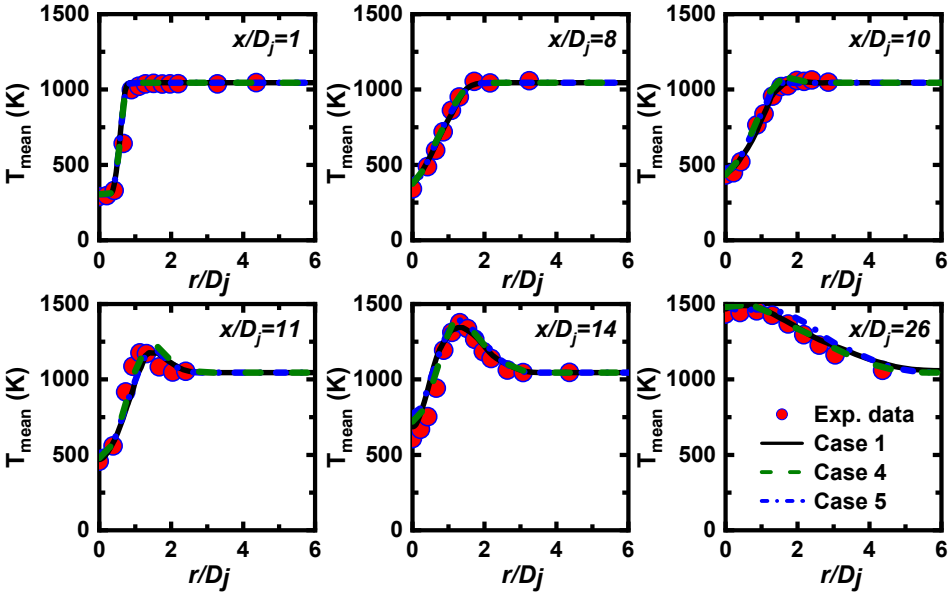

Fig. 17 – Radial profiles of mean temperature with various convection schemes. Experimental data from Ref. [7].

The distributions of the mean and RMS conditional scalar dissipation rate in mixture fraction space at the same probe for Cases 1 – 3 are showed in Fig. 16. They are collected from the CMC resolution (i.e. $\widetilde{N|\eta}^{CMC}$) and correspond to Eq. (16). The data were averaged from $t = 0.005$ s–0.012 s. Obviously, the mean and RMS of scalar dissipation rate ($\widetilde{N|\eta}^{CMC}$) in the whole mixture fraction range are the largest in Case 1, while they are the smallest in Case 3. The reader should be reminded that in Case 2 the identical LES and CMC meshes are used, and hence the data averaging from LES to CMC mesh (i.e. Eq. (16)) is actually not enforced. Nevertheless, the coarse CMC mesh leads to the deviations of $\widetilde{N|\eta}^{CMC}$ relative to that from Case 2. Relatively low or intermediate scalar dissipation rate indicates a high propensity for the mixture to be ignited, as discussed by Mastorakos [48]. This trend has also been demonstrated in Fig. 15. It is also found due to the various mesh resolutions, the differences in $N|\eta_{mean}$ are smaller than differences in $N|\eta_{rms}$, and the difference in mean values from the Cases 1, 2 and 3 is less obvious. Besides, the finest mesh does not lead to a smallest conditionally averaged dissipation rate ($\widetilde{N|\eta}$), and the reason could be attributed to the calculations of $\widetilde{N|\eta}$. As described in Sections Large eddy simulation and Conditional moment closure model, the $\widetilde{N|\eta}$ in one CMC cell is integrated from its host LES cells. However, the numbers of LES cells in one CMC cell among the three cases are not the same. Moreover, since the probe is close to the flame base, strong unsteadiness and spatial variations of the conditional quantities may exist.

Effects of numerical scheme for CMC equations

Fig. 17 shows the radial profiles of the mean temperature at different axial locations. Cases 1, 4 and 5 respectively correspond to three various convection schemes for the CMC equations, i.e. blended UD/CD schemes with blending factor $\gamma = 0.7$ and 0.5, as well as UD scheme. In general, there are limited differences between the measured and the simulated mean temperature with three convection schemes. An in-depth observation on Fig. 17 shows that the mean temperatures predicted with blend UD/CD schemes are smaller than those calculated with UD scheme at $x/D_j = 26$. This is because the UD scheme is more dissipative than the blend ones, especially at further downstream locations (e.g. $x/D_j = 26$) where the mesh size is larger. The

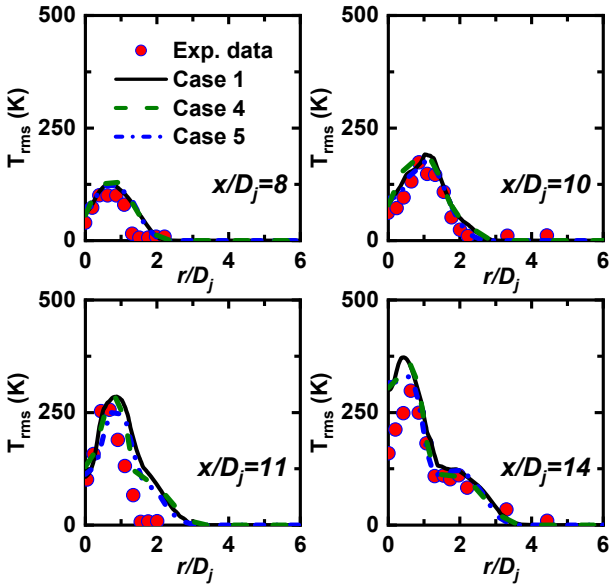

Fig. 18 – Radial profiles of temperature RMS with different convection schemes. Experimental data from Ref. [7].

Please cite this article as: Li G et al., Large eddy simulation and finite-volume conditional moment closure modelling of a turbulent lifted H_2/N_2 flame, International Journal of Hydrogen Energy, https://doi.org/10.1016/j.ijhydene.2021.09.209

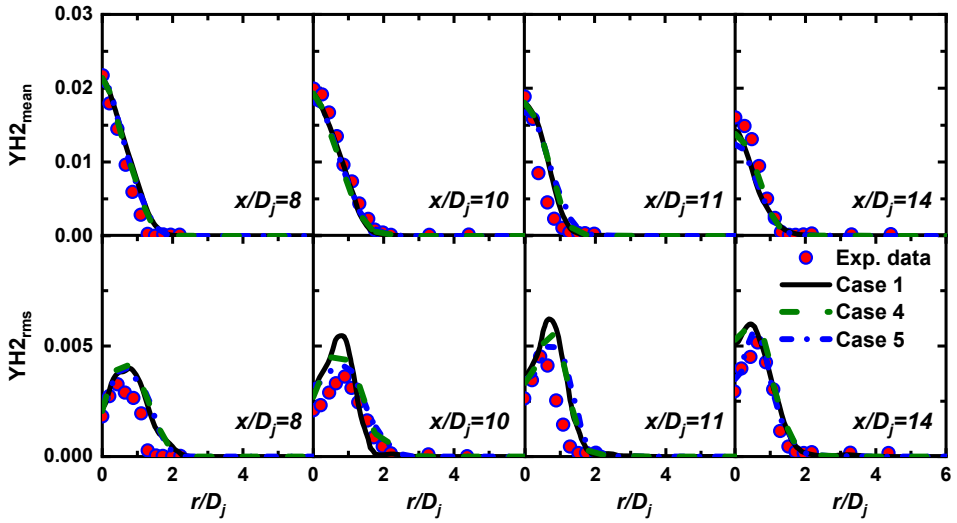

Fig. 19 – Radial profiles of mean and RMS of H_2 mass fraction in Cases 1, 4 and 5 at four axial locations. Experimental data from Ref. [7].

radial distributions of temperature RMS values at four locations are presented in Fig. 18. The variations of the temperature RMS values are all reproduced satisfactorily with the three schemes, except a slight overestimation at $x/D_j = 11$ near the flame base.

The mean and RMS of H_2 mass fraction computed with three convection schemes in Cases 1, 4 and 5 are in good agreement with the experimental data, as showed in Fig. 19. The predictions of the RMS of H_2 mass fraction show slight difference for the three cases, especially at $x/D_j = 10$ and 11 where the flame base locates. The fluctuations of H_2 mass fraction in Case 1 have the largest deviation from the measurements. Fig. 20 shows that the deviations of OH mass fraction between the simulations and measurements gradually increase from $x/D_j = 10$ and then decrease at the downstream of the flow ($x/D_j = 14$). This can be ascribed to the slightly overestimated lift-off heights calculated in Case 1, 4 and 5. Similar to the predictions of H_2 mass fraction, the fluctuations of OH mass fraction also show a larger deviation from the measurements in Case 1 compared with Cases 4 and 5.

The interactions between the CMC cells may considerably affect the predictions of the flame dynamics [21,28]. As reported in Refs. [21,23], flame autoignition mechanism can be clarified by the instantaneous magnitudes of different terms in the CMC equations. The analysis of the highly unsteady and localized auto-ignition process near the flame base is based on the instantaneous ones. Therefore, the budgets of CMC terms

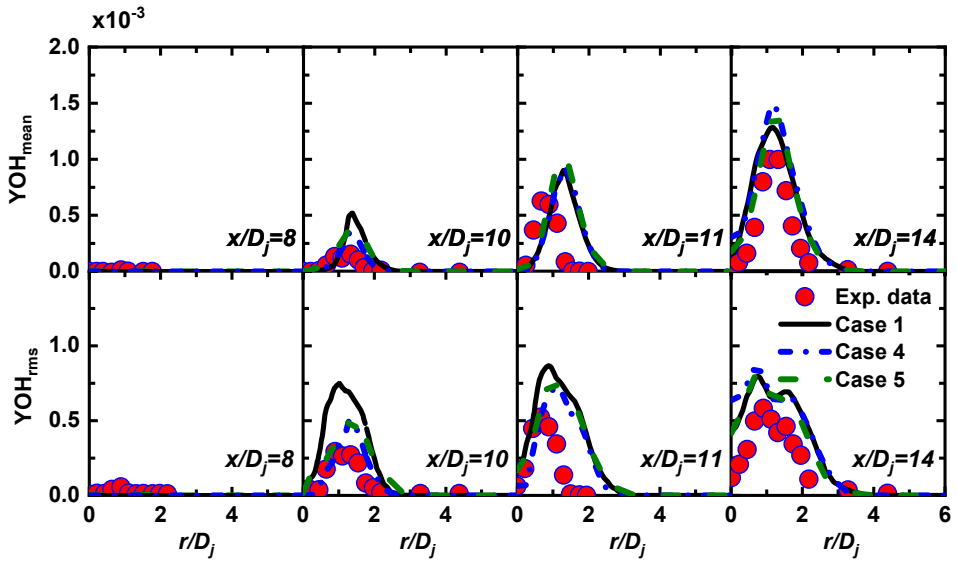

Fig. 20 – Radial profiles of mean and RMS of OH mass fraction in Cases 1, 4 and 5 at four axial locations. Experimental data from Ref. [7].

Please cite this article as: Li G et al., Large eddy simulation and finite-volume conditional moment closure modelling of a turbulent lifted H_2/N_2 flame, International Journal of Hydrogen Energy, https://doi.org/10.1016/j.ijhydene.2021.09.209

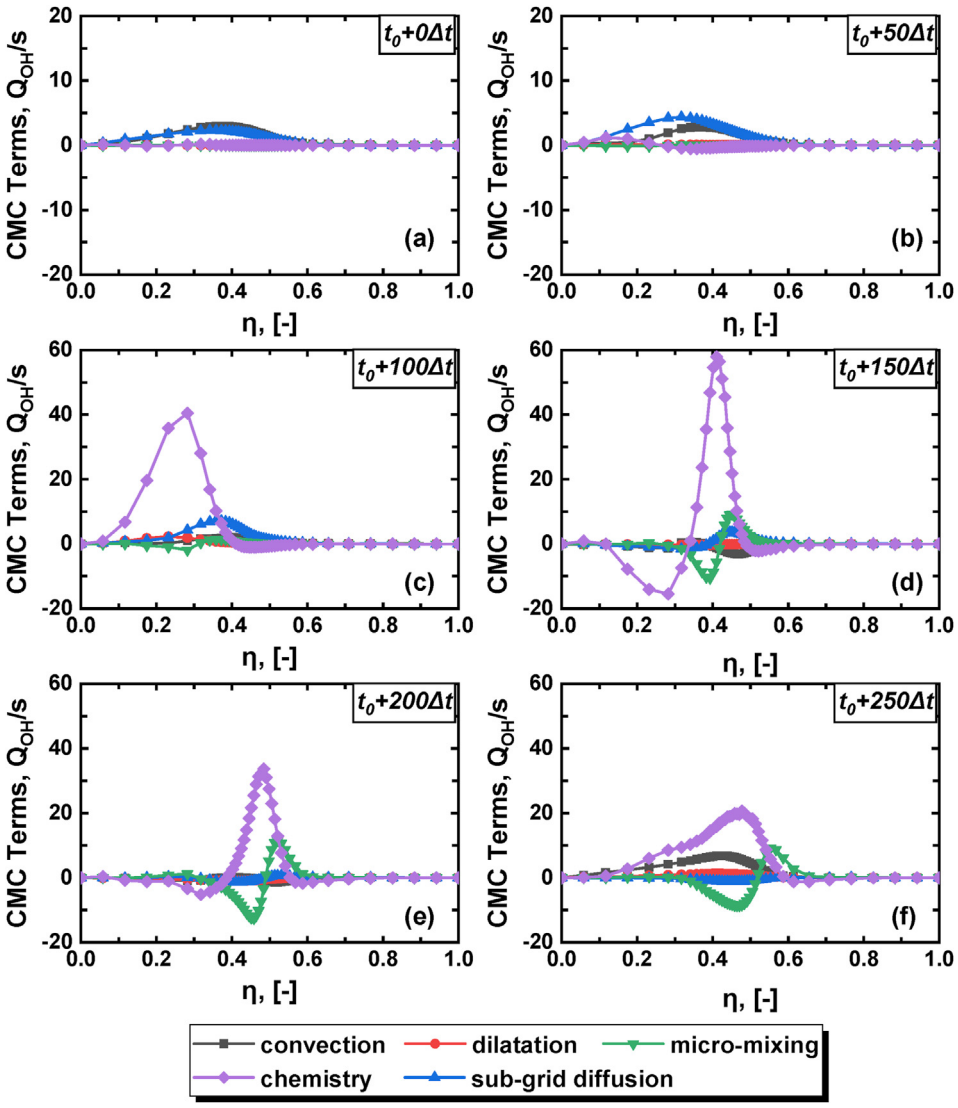

Fig. 21 – Budgets of the CMC terms for OH mass fraction equation at the probe ($x/D_j = 11$, $y/D_j = 1.4$, $z/D_j = 0$) for Case 1.

(T_1, T_2, T_3, T_4 and T_5) in mixture fraction space will be analyzed in one CMC cell ($x/D_j = 11$, $y/D_j = 1.4$, $z/D_j = 0$, marked in Fig. 4a) near the flame base. We select six time instants during the auto-ignition process with the time interval of 0.00005 s, and the first instant is termed as t_0 as shown in Figs. 21–23. The contributions of the CMC terms on the conditionally filtered OH mass fraction ($\widetilde{Y_{OH}|\eta}$) in Case 1 (blend factor $\gamma = 0.7$) are shown in Fig. 21, where t_0 corresponds to the time of 0.0099s. It is observed that the dilatation, micro-mixing and chemistry terms, i.e. $T_2 = Q_\alpha \widetilde{\frac{\partial u_k|\eta}{\partial x_k}}$, $T_3 = \widetilde{N|\eta} \frac{\partial^2 Q_\alpha}{\partial^2 \eta}$ and $T_4 =$, are close to zero at $t = t_0$, while the convection ($T_1 = \widetilde{\omega_\alpha|\eta}$) and sub-grid diffusion terms ($T_5 = \widetilde{\frac{\partial(u_k|\eta Q_\alpha)}{\partial x_k}}$) have similar magnitudes at t_0. Since the T_1 and T_5 are respectively at the left and right sides of Eq. (11), production of OH radical is negligible at t_0. The contribution of the chemistry term merges from $t = t_0 + 50\frac{\partial}{\partial x_k}\left(D_t \frac{\partial Q_\alpha}{\partial x_k}\right)$ (Fig. 21b), and progressively increases with time until the flame becomes stable after 200Δt. The micro-mixing term exhibits its contribution after 100Δt, and shows an opposite effect on Δt compared with the chemistry term (T_4), particularly at $t = t_0 + 250\widetilde{Y_{OH}|\eta}$. The above phenomenon is also reported in Ref. [18]. Both the sub-grid scale diffusion and convection terms have finite effects in Fig. 21(a)(d). The convection and diffusion in physical space contribute to the interactions between fresh CMC cell and burning one. However, these contributions are not comparable with that of chemistry term when the maximum temperature in mixture fraction space arrives 1200 K as showed in Fig. 21(c) and (d).

Fig. 22 shows the balance between different CMC terms for Case 4, where the blended UD/CD scheme with the

Please cite this article as: Li G et al., Large eddy simulation and finite-volume conditional moment closure modelling of a turbulent lifted H_2/N_2 flame, International Journal of Hydrogen Energy, https://doi.org/10.1016/j.ijhydene.2021.09.209

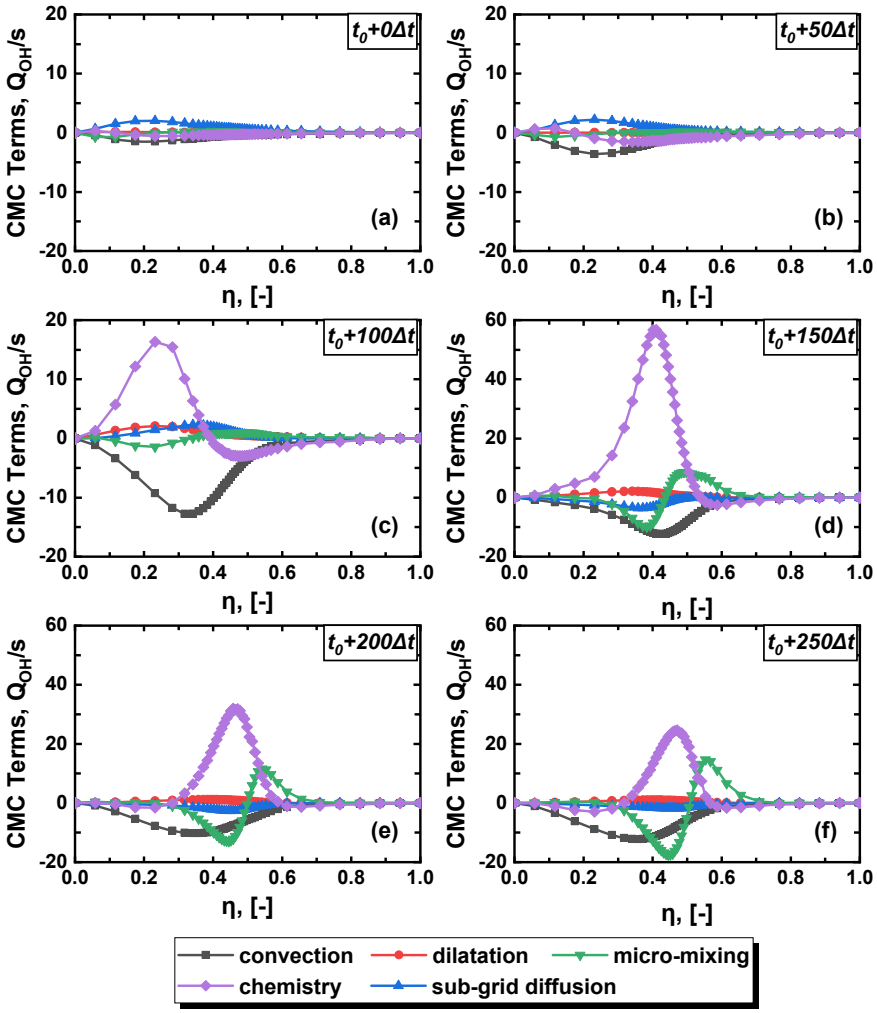

Fig. 22 – Budgets of the CMC terms for OH mass fraction equation at the probe ($x/D_j = 11$, $y/D_j = 1.4$, $z/D_j = 0$) for Case 4.

blending factor of 0.5 is used. The time 0.0134 s is selected as the initial time t_0. The contributions of chemistry and micro-mixing terms are similar to that in Case 1 (shown in Fig. 21). The dilatation and sub-grid scale diffusion terms are relatively small, which are basically similar to the counterparts in Case 1. However, the convection – term is different from that in Case 1 where the blending factor is 0.7. It is seen that the contributions of the convection term are always negative during the whole ignition process, and the effects of convection showed in Fig. 21(c)–(f) become more evident than those in Fig. 21(c)–(f). This indicates that the convection schemes with different blending factors influence the contributions of the convective transport. Additionally, the maximum magnitudes of the contribution of the convection term is about 13 observed in Fig. 22(c), which is larger than that in Case 1.

Likewise, the budget analysis is also conducted for Case 5 in Fig. 23, in which the upwind scheme is used. The initial time is $t_0 = 0.00995$ s. Similar to the budget analysis for Cases 4 and 5, the effects of dilatation and sub-grid scale diffusion terms in Case 5 are small during the auto-ignition process, while the chemistry term plays an important role on the flame development. The contributions of the micro-mixing term in Fig. 23 are small and not sufficient to compete with the chemistry term, which is different from Cases 1 and 4. In Cases 1 and 4, the micro-mixing term has almost the same magnitude with the chemistry term when the fully burning state is reached. For the convection term, the absolute value of the maximum contribution of the convection term is about 20 observed in Fig. 23(e), the largest one among those in Cases 1, 4 and 5.

As mentioned in Section Finite volume discretization of CMC equations, one CMC cell contains numerous CMC faces, through which the numerical flux enters or leaves the enclosed CMC cell. This would considerably affect the local flame structures and may induce strong unsteadiness of conditional flame structure. The instantaneous convective flux of stoichiometric OH mass fraction from individual CMC faces are illustrated in Fig. 24. Results are extracted from the same probed CMC cell at $t = t_0+50\Delta t$ in Figs. 21(b), 22(b) and

Please cite this article as: Li G et al., Large eddy simulation and finite-volume conditional moment closure modelling of a turbulent lifted H_2/N_2 flame, International Journal of Hydrogen Energy, https://doi.org/10.1016/j.ijhydene.2021.09.209

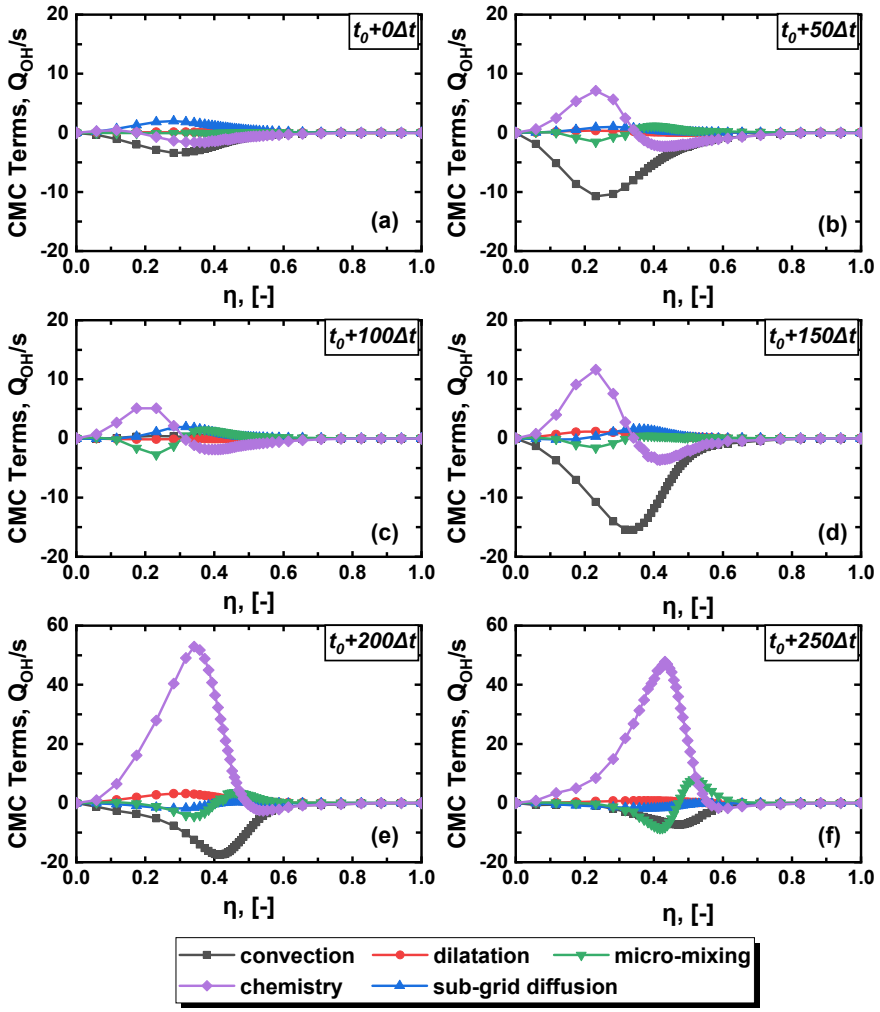

Fig. 23 – Budgets of the CMC terms for OH mass fraction equation at the probe ($x/D_j = 11$, $y/D_j = 1.4$, $z/D_j = 0$) for Case 5.

23(b). The negative sign in Fig. 24 means influx of the numerical flux for the CMC cell, while the positive one means the outflux. This CMC cell has 21 CMC faces, and each face is shared by two neighboring CMC cells. The convective flux of blended scheme (Cases 1 and 4) at the CMC faces have a similar trend: the convective flux at most CMC faces are small, and only one face plays a dominant role in convection transport between the neighboring cells. While for the UD scheme (Case 5), most convective fluxes are negative, and there are about half of the CMC faces showing finite and comparable contributions. This further indicates that the reactivity of a CMC cell is more easily to be affected by its neighbors when UD scheme is used.

Besides, OH mass fractions at the stoichiometric mixture fraction ($\widetilde{Y_{OH}|\xi_{st}}$) for the neighboring CMC cells (which share one CMC face with the current one) are also showed as the numbers near the bars in Fig. 24. For Case 5, the stoichiometric mass fraction $\widetilde{Y_{OH}|\xi_{st}}$ of the current CMC cell is 1.1×10^{-4}, while $\widetilde{Y_{OH}|\xi_{st}}$ at its neighbor CMC cells are 4.1×10^{-4} for face 11, 2.0×10^{-4} for face 4 and 9.1×10^{-5} for face 1, respectively. These finite values of $\widetilde{Y_{OH}|\xi_{st}}$ mean that the neighboring CMC cells are under burning state. Therefore, the gross convective fluxes may make the current CMC cell have the propensity to be ignited. For Case 1, $\widetilde{Y_{OH}|\xi_{st}}$ of the current CMC cell is 1.4×10^{-5}, while the largest $\widetilde{Y_{OH}|\xi_{st}}$ at its neighbor CMC cell is 2.1×10^{-3} for face 11. Hence the convective fluxes would not instantaneously facilitate the ignition of the current cell. Similar to Case 1, the instantaneous fluxes in Case 4 also make negative contributions to autoignition in the current cell, as the $\widetilde{Y_{OH}|\xi_{st}}$ is 4.5×10^{-5} at this cell, while $Y_{OH}|\xi_{st}$ at its neighbor CMC cell is 3.4×10^{-4} for face 10. However, in Case 1 and 4, this CMC cell still proceeds towards fully burning conditions due to the continuous interactions between the various flame structures in physical space, as illustrated in Figs. 21 and 22.

Please cite this article as: Li G et al., Large eddy simulation and finite-volume conditional moment closure modelling of a turbulent lifted H_2/N_2 flame, International Journal of Hydrogen Energy, https://doi.org/10.1016/j.ijhydene.2021.09.209

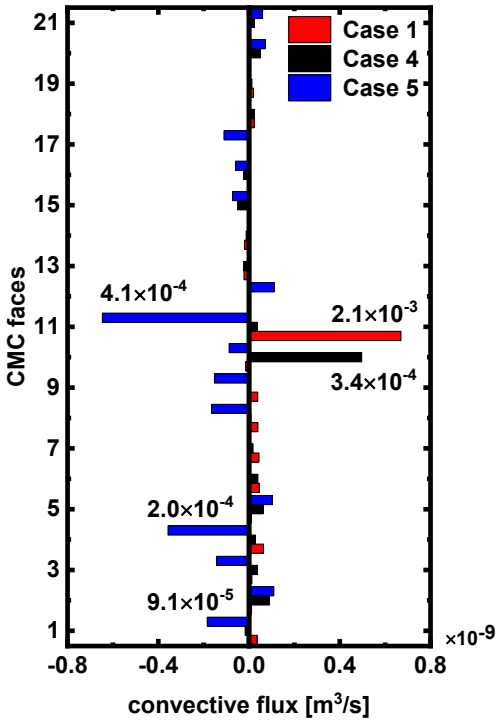

Fig. 24 – Convective flux across each face of the CMC cell at the probe ($x/D_j = 11$, $y/D_j = 1.4$, $z/D_j = 0$) for Cases 1, 4 and 5. Numbers near the bars are to the OH mass fraction at the stoichiometric mixture fraction ($Y_{OH}|\xi_{st}$) for the neighboring CMC cells.

Conclusion

The LES – CMC simulations are performed for a lifted H_2/N_2 jet in turbulent vitiated co-flow with detailed chemical mechanism. The effects of mesh resolution and numerical scheme of the finite volume CMC model on predictions of reactive scalars and unsteady flame behaviors are analyzed in this work.

The comparisons between the measured and predicted radial distributions of temperature, mixture fraction and species mass fractions at different locations show that the LES – CMC approach has a better performance with the finer CMC mesh. Besides, the lift-off height is underestimated if the CMC mesh resolution is large. However, excessive refinement of the CMC mesh is unable to further improve the prediction accuracy. The time sequences of the most reactive and stoichiometric OH mass fractions in different CMC meshes illustrates that the finer CMC mesh is capable of capturing more unsteady details than the coarser CMC mesh. The coarser CMC mesh has lower conditional scalar dissipation rate, which promotes the ignition of the lifted flame.

Furthermore, the effects of convection schemes for the finite volume CMC equations on the reactive scalar profiles in physical and mixture fraction space are also investigated. Comparisons against the experimental data indicate that the influences of various convection schemes on the time-averaged temperature, mixture fraction and species mass fraction are negligible. The fluctuations of H_2 and OH mass fractions show larger deviations from the measurements with hybrid upwind and central differencing scheme, especially around the flame base. The budget analysis illustrates the magnitudes of the individual CMC terms (i.e. T_1-T_5 in Eq. (11)) at various instants. The results suggest that the contributions of the convection term increase with the blending factor, and the absolute value of the maximum contributions of convection term is obtained with the upwind scheme. It is also shown that the instantaneous convective flux of stoichiometric OH mass fraction from individual CMC faces is considerably affected by the convection scheme. The reactivity of a CMC cell is more easily to be affected by its neighbors with upwind scheme.

Based on our results, the recommended ratio of the CFD cells to the CMC cells is 3.7 to 1 which is estimated from the base case (Case 1), to have a correct prediction of the reactive scalars in physical and mixture fraction space for the turbulent lifted hydrogen flame. The reasonable refinement of CMC mesh near the flame base is expected to improve the prediction, and the desirable size of the CMC cells is identical with the CFD cells in the region so that the errors caused by the integration of reactive scalars between the two meshes can be minimized. Moreover, to obtain a better prediction of the fluctuations of H_2 and OH mass fraction for the lifted hydrogen flame, especially around the flame base, the upwind convection scheme is recommended, while the blend UD/CD scheme is shown to get a better prediction of the mean temperatures in the downstream of the flame.

Declaration of competing interest

The authors declare that they have no known competing financial interests or personal relationships that could have appeared to influence the work reported in this paper.

Acknowledgement

This work used the ASPIRE 1 Cluster from National Supercomputing Center, Singapore (https://www.nscc.sg/). GL is sponsored by The CSC Scholarship (201806020055). HZ is supported by Singapore Ministry of Education Tier 1 grant (R-265-000-653-114). Dr. Bertrand Naud from CIEMAT is acknowledged for sharing the experimental data and post-processing routines. The authors thank the anonymous reviewers for the helpful comments.

Appendix A. Sensitivity of reactive scalar statistics to LES mesh resolution

Fig. A1 shows the radial distributions of the time-averaged temperature predicted with two LES meshes (i.e. 260 × 90 × 72 and 134 × 54 × 42) at six axial locations. Note that the second mesh is used in the above analysis and for brevity they are termed as M1 and M2, respectively. Here the CMC mesh consists of 94 × 36 × 24 cells. It is found that the mean temperature from two meshes have good agreements with the measurements at all the locations, although the time-averaged temperature is slightly over-predicted by the fine LES mesh (i.e. M1) in the jet centerline at $x/D_j = 14$. The temperature RMS from the two meshes are compared against the measurements at four positions in Fig. A2. The two results are in good accordance with the experimental data at $x/D_j = 8$ and 10, while the temperature RMS at $x/D_j = 11$ and 14 are overestimated in both M1 and M2. In general, the results from two LES meshes have negligible differences regarding the temperature statistics. Similar tendencies can also be found from the species mass fraction statistics.

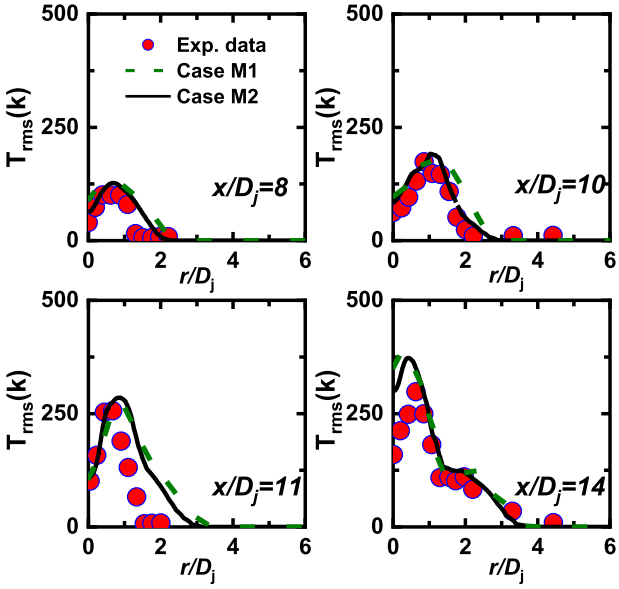

Fig. A2 – Radial profiles of the temperature RMS from two LES meshes.

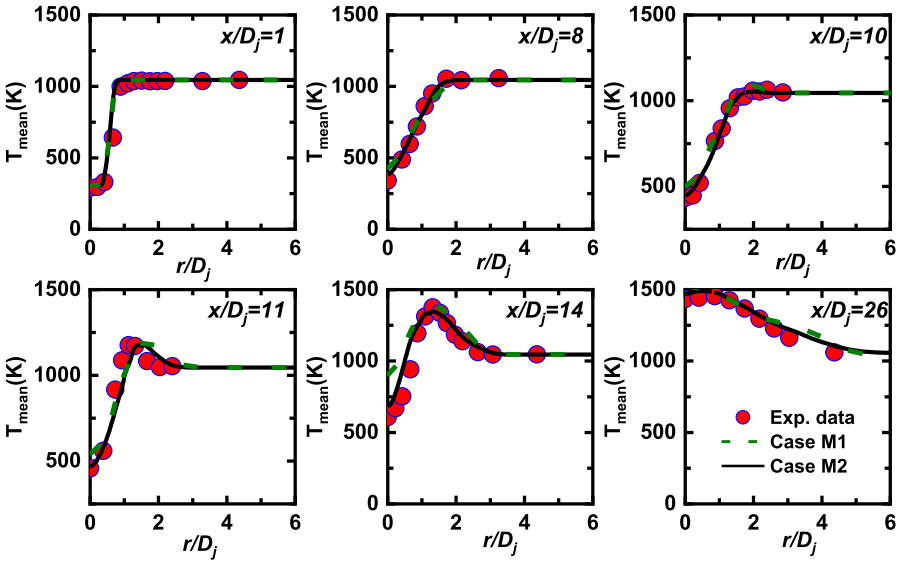

Fig. A1 – Radial profiles of the time-averaged temperatures from two LES meshes.

Please cite this article as: Li G et al., Large eddy simulation and finite-volume conditional moment closure modelling of a turbulent lifted H_2/N_2 flame, International Journal of Hydrogen Energy, https://doi.org/10.1016/j.ijhydene.2021.09.209

Fig. A3 shows the mean and RMS of mixture fraction at $x/D_j = 8$, 10, 11, and 14 from two LES meshes. The distributions of the mean mixture fraction are predicted generally well in both LES meshes at all the locations. Furthermore, the mixture fractions along the centerline at $x/D_j = 14$ are underestimated with M1. This may be related to the over-prediction of mean temperature at the same location in Fig. A1. Moreover, the RMS of mixture fraction at all the shown locations are well reproduced by the two meshes, in spite of a slight overestimation at $x/D_j = 11$. One can therefore conclude from Figs. A1–A3 that the results from both LES meshes have good agreements with the experimental data, and the mesh (i.e. M2) used in the foregoing studies are sufficient.

Appendix B. LES mesh resolution compared with turbulent length scales

The integral length scale (L_t) and Kolmogorov scale (η_k) can be estimated as [62]:

$$L_t \approx D_j(1 + B \cdot x) \tag{B1}$$

$$\eta_k = L_t Re_t^{-3/4} \tag{B2}$$

where D_j is the diameter of a round jet, $B \approx 0.09$ is the expansion rate of the jet [56] and x is the axial coordinate. $Re_t = u'L_t/\upsilon$ is the local turbulent Reynolds number [63] obtained using the RMS field of velocity u' from the resolved field and the kinematic viscosity υ.

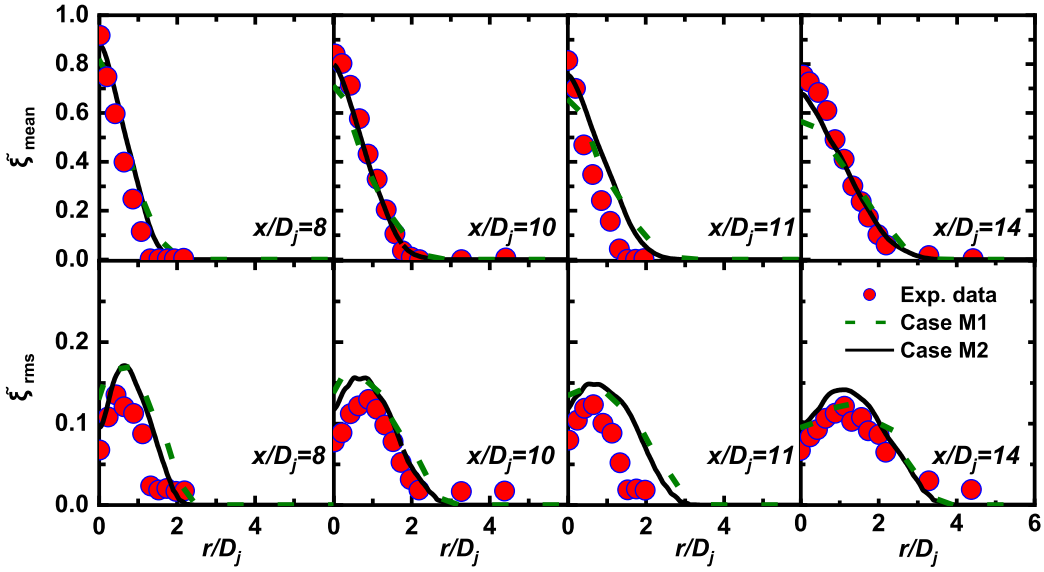

Fig. A3 – Radial profiles of mean (top) and RMS (bottom) of mixture fraction from two LES meshes.

Please cite this article as: Li G et al., Large eddy simulation and finite-volume conditional moment closure modelling of a turbulent lifted H_2/N_2 flame, International Journal of Hydrogen Energy, https://doi.org/10.1016/j.ijhydene.2021.09.209

Based on Eqs. (B1) and (B2), we compare the nominal LES cell size Δ with the integral length scale L_t and Kolmogorov scale η_k from Case 1 (see Table 2), which are shown in Fig. B1. It is observed that for $x < 20D_j$, the grid size represents less than 8% of the integral length scale and about 10–20 times greater than the Kolmogorov length scale. Since other cases in Table 2 use the same LES resolution, and hence all our simulations are supposed to be sufficient to capture the turbulence scales of large eddies.

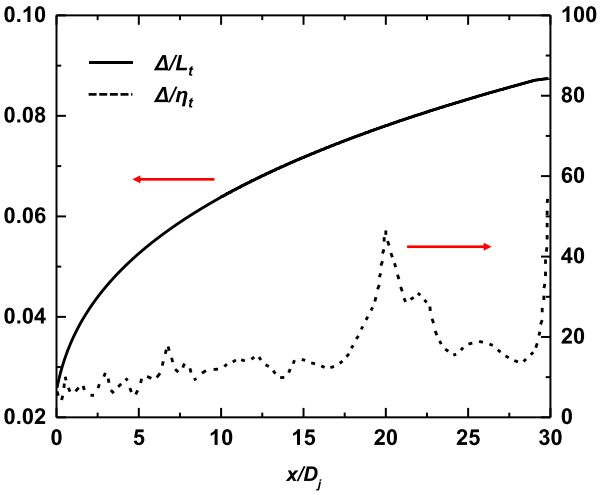

Fig. B1 – Nominal LES mesh size (Δ) compared to the integral scale (L_t) and the Kolmogorov scale (η_k) on the jet axis.

Appendix C. Fraction of unresolved turbulent kinetic energy

According to Pope [64], at least 80% of the total turbulent kinetic energy should be resolved in an LES. The fraction of unresolved kinetic energy is estimated from

$$Me = \frac{k_{sgs}}{k_{RES} + k_{sgs}}, \tag{C1}$$

where k_{sgs} is the sub-grid turbulent kinetic energy and k_{RES} is the resolved turbulent kinetic energy.

Fig. C1 shows the distribution of *Me* in different LES meshes, using the data with hydrogen mass fraction $\tilde{Y}_{H2} > 0.001$. The coarse and fine meshes have 260 × 90 × 72 and 134 × 54 × 42 cells, respectively. The same CMC mesh is used, which consists of 94 × 36 × 24 cells. It can be found that the probability density distributions with *Me* < 0.2 are about 0.86 and 0.96 from the coarse and fine meshes, respectively. The results in Fig. C1 further confirm the sufficiency of the LES mesh resolution used in this study.

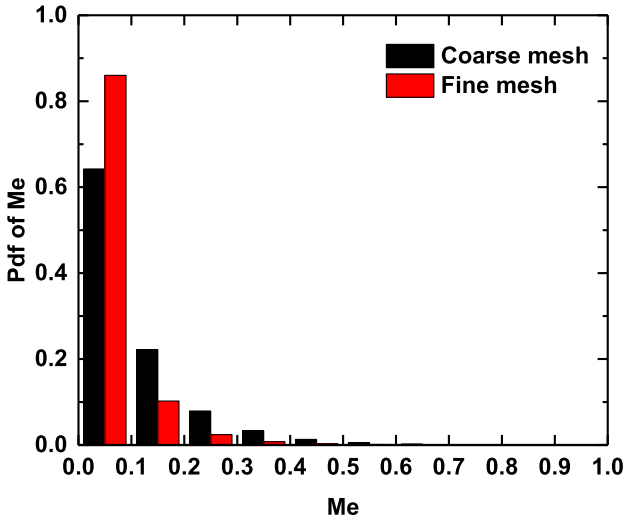

Fig. C1 – Probability density function of *Me* with different LES meshes.

REFERENCES

[1] Lawn CJ. Lifted flames on fuel jets in co-flowing air. Prog Energy Combust Sci 2009;35(1):1–30.
[2] Lyons KM. Toward an understanding of the stabilization mechanisms of lifted turbulent jet flames: Experiments. Prog Energy Combust Sci 2007;33(2):211–31.
[3] Pitts WM. Assessment of theories for the behavior and blowout of lifted turbulent jet diffusion flames. Symp Combust Proc 1989;22(1):809–16.
[4] Huang Z, Cleary MJ, Zhang H. Application of the sparse-Lagrangian multiple mapping conditioning approach to a model supersonic combustor. Phys Fluids 2020;32(10):105120.
[5] Klimenko AY, Pope S. The modeling of turbulent reactive flows based on multiple mapping conditioning. Phys Fluids 2003;15(7):1907–25.
[6] Guiberti TF, Boyette WR, Krishna Y, Roberts WL, Masri AR, Magnotti G. Assessment of the stabilization mechanisms of turbulent lifted jet flames at elevated pressure using combined 2-D diagnostics. Combust Flame 2020;214:323–35.
[7] Cabra R, Myhrvold T, Chen JY, Dibble RW, Karpetis AN, Barlow RS. Simultaneous laser Raman–Rayleigh-lif measurements and numerical modeling results of a lifted turbulent H2/N2 jet flame in a vitiated coflow. Proc Combust Inst 2002;29(2):1881–8.
[8] Wu Z, Masri AR, Bilger RW. An experimental investigation of the turbulence structure of a lifted H2/N2 jet flame in a vitiated co-flow. Flow Turbul Combust 2006;76(1):61–81.
[9] Markides CN, Mastorakos E. An experimental study of hydrogen autoignition in a turbulent co-flow of heated air. Proc Combust Inst 2005;30(1):883–91.

Please cite this article as: Li G et al., Large eddy simulation and finite-volume conditional moment closure modelling of a turbulent lifted H_2/N_2 flame, International Journal of Hydrogen Energy, https://doi.org/10.1016/j.ijhydene.2021.09.209

[10] Leung T, Wierzba I. The effect of co-flow stream velocity on turbulent non-premixed jet flame stability. Proc Combust Inst 2009;32(2):1671–8.
[11] Khateeb AA, Guiberti TF, Zhu X, Younes M, Jamal A, Roberts WL. Stability limits and NO emissions of technically-premixed ammonia-hydrogen-nitrogen-air swirl flames. Int J Hydrogen Energy 2020;45(41):22008–18.
[12] Kim W, Namba T, Johzaki T, Endo T. Self-similar propagation of spherically expanding flames in lean hydrogen–air mixtures. Int J Hydrogen Energy 2020;45(46):25608–14.
[13] Guo S, Wang J, Zhang W, Zhang M, Huang Z. Effect of hydrogen enrichment on swirl/bluff-body lean premixed flame stabilization. Int J Hydrogen Energy 2020;45(18):10906–19.
[14] Huang Z, Zhang H. Numerical investigations of mixed supersonic and subsonic combustion modes in a model combustor. Int J Hydrogen Energy 2020;45(1):1045–60.
[15] Zhu R, Zhao M, Zhang H. Numerical simulation of flame acceleration and deflagration-to-detonation transition in ammonia-hydrogen–oxygen mixtures. Int J Hydrogen Energy 2021;46(1):1273–87.
[16] Devaud CB, Bray KNC. Assessment of the applicability of conditional moment closure to a lifted turbulent flame: first order model. Combust Flame 2003;132(1):102–14.
[17] Roy RN, Kumar S, Sreedhara S. A new approach to model turbulent lifted CH4/air flame issuing in a vitiated coflow using conditional moment closure coupled with an extinction model. Combust Flame 2014;161(1):197–209.
[18] Kim IS, Mastorakos E. Simulations of turbulent lifted jet flames with two-dimensional conditional moment closure. Proc Combust Inst 2005;30(1):911–8.
[19] Stanković I, Triantafyllidis A, Mastorakos E, Lacor C, Merci B. Simulation of hydrogen auto-ignition in a turbulent Co-flow of heated air with LES and CMC approach. Flow, Turbul Combust 2011;86(3):689–710.
[20] Stanković I, Mastorakos E, Merci B. LES-CMC simulations of different auto-ignition regimes of hydrogen in a hot turbulent air Co-flow. Flow, Turbul Combust 2013;90(3):583–604.
[21] Navarro-Martinez S, Kronenburg A. Flame stabilization mechanisms in lifted flames. Flow Turbul Combust 2011;87(2):377–406.
[22] Patwardhan S, De S, Lakshmisha K, Bn R. CMC simulations of lifted turbulent jet flame in a vitiated coflow. Proc Combust Inst 2009;32.
[23] Tyliszczak A. Assessment of implementation variants of conditional scalar dissipation rate in LES-CMC simulation of auto-ignition of hydrogen jet. Arch Mech 2013;65:97–129.
[24] Rosiak A, Tyliszczak A. LES-CMC simulations of a turbulent hydrogen jet in oxy-combustion regimes. Int J Hydrogen Energy 2016;41(22):9705–17.
[25] Zhang H, Garmory A, Cavaliere DE, Mastorakos E. Large eddy Simulation/Conditional Moment Closure modeling of swirl-stabilized non-premixed flames with local extinction. Proc Combust Inst 2015;35(2):1167–74.
[26] Garmory A, Mastorakos E. Numerical simulation of oxy-fuel jet flames using unstructured LES–CMC. Proc Combust Inst 2015;35(2):1207–14.
[27] Zhang H. Extinction in turbulent swirling non-premixed flames. University of Cambridge; 2015.
[28] Zhang H, Mastorakos E. Prediction of global extinction conditions and dynamics in swirling non-premixed flames using LES/CMC modelling. Flow, Turbul Combust 2016;96(4):863–89.
[29] Zhang H, Mastorakos E. LES/CMC modelling of a gas turbine model combustor with quick fuel mixing. Flow Turbul Combust 2019;102(4):909–30.
[30] Zhang H, Mastorakos E. Modelling local extinction in Sydney swirling non-premixed flames with LES/CMC. Proc Combust Inst 2017;36(2):1669–76.
[31] Huangwei Z, Giusti A, Mastorakos E. LES/CMC modelling of ignition and flame propagation in a non-premixed methane jet. Proc Combust Inst 2019;37(2):2125–32.
[32] Poinsot T, Veynante D. Theoretical and numerical combustion. RT Edwards, Inc.; 2005.
[33] Smagorinsky J. General circulation experiments with the primitive equations: I. The basic experiment. Mon Weather Rev 1963;91(3):99–164.
[34] Farrace D, Chung K, Bolla M, Wright YM, Boulouchos K, Mastorakos E. A LES-CMC formulation for premixed flames including differential diffusion. Combust Theor Model 2018;22(3):411–31.
[35] Ma M-C, Devaud CB. A conditional moment closure (CMC) formulation including differential diffusion applied to a non-premixed hydrogen–air flame. Combust Flame 2015;162(1):144–58.
[36] Branley N, Jones WP. Large eddy simulation of a turbulent non-premixed flame. Combust Flame 2001;127(1):1914–34.
[37] Pierce CD, Moin P. A dynamic model for subgrid-scale variance and dissipation rate of a conserved scalar. Phys Fluids 1998;10(12):3041–4.
[38] Pera C, Réveillon J, Vervisch L, Domingo P. Modeling subgrid scale mixture fraction variance in LES of evaporating spray. Combust Flame 2006;146(4):635–48.
[39] Jiménez C, Ducros F, Cuenot B, Bédat B. Subgrid scale variance and dissipation of a scalar field in large eddy simulations. Phys Fluids 2001;13(6):1748–54.
[40] Triantafyllidis A, Mastorakos E. Implementation issues of the conditional moment closure model in large eddy simulations. Flow, Turbul Combust 2010;84(3):481–512.
[41] Bushe WK, Steiner H. Conditional moment closure for large eddy simulation of nonpremixed turbulent reacting flows. Phys Fluids 1999;11(7):1896–906.
[42] Navarro-Martinez S, Kronenburg A, Di Mare F. Conditional moment closure for large eddy simulations. Flow, Turbul Combust 2005;75(1–4):245–74.
[43] Navarro-Martinez S, Kronenburg A. LES-CMC simulations of a turbulent bluff-body flame. Proc Combust Inst 2007;31(2):1721–8.
[44] Kim SH, Pitsch H. Mixing characteristics and structure of a turbulent jet diffusion flame stabilized on a bluff-body. Phys Fluids 2006;18(7):075103.
[45] O'Brien EE, Jiang TL. The conditional dissipation rate of an initially binary scalar in homogeneous turbulence. Phys Fluid Fluid Dynam 1991;3(12):3121–3.
[46] Versteeg HK, Malalasekera W. An introduction to computational fluid dynamics: the finite volume method. Pearson education; 2007.
[47] Bilger RW, Stårner SH, Kee RJ. On reduced mechanisms for methane - air combustion in nonpremixed flames. Combust Flame 1990;80(2):135–49.
[48] Mastorakos E. Ignition of turbulent non-premixed flames. Prog Energy Combust Sci 2009;35(1):57–97.
[49] K N, H E. Method of random spots for generation of synthetic inhomogeneous turbulent fields with prescribed autocorrelation functions. Commun Numer Methods Eng 2007;23(1):35–43.
[50] Masri AR, Pope SB, Dally BB. Probability density function computations of a strongly swirling nonpremixed flame stabilized on a new burner. Proc Combust Inst 2000;28(1):123–31.
[51] Brown PN, Hindmarsh AC. Reduced storage matrix methods in stiff ODE systems. Appl Math Comput 1989;31:40–91.

Please cite this article as: Li G et al., Large eddy simulation and finite-volume conditional moment closure modelling of a turbulent lifted H_2/N_2 flame, International Journal of Hydrogen Energy, https://doi.org/10.1016/j.ijhydene.2021.09.209

[52] Li J, Zhao Z, Kazakov A, Dryer FL. An updated comprehensive kinetic model of hydrogen combustion. Int J Chem Kinet 2004;36(10):566–75.
[53] Zhang F, Yu R, Bai X, Yao M, Peng Z. Direct numerical simulation of flame/spontaneous ignition interaction fueled with hydrogen under SACI engine conditions. Int J Hydrogen Energy 2017;42(6):3842–52.
[54] Lu L, Ren Z, Lantz S, Raman V, Pope SB, Pitsch H. Investigation of strategies for the parallel implementation of ISAT in LES/FDF/ISAT computations. Fourth joint meeting of the US Sections of the Combustion Institute. Philadelphia, PA: Drexel University; 2005. p. 20–3.
[55] Suh HK, Lee CS. Effect of cavitation in nozzle orifice on the diesel fuel atomization characteristics. Int J Heat Fluid Flow 2008;29(4):1001–9.
[56] Cao RR, Pope SB, Masri AR. Turbulent lifted flames in a vitiated coflow investigated using joint PDF calculations. Combust Flame 2005;142(4):438–53.
[57] Gordon RL, Masri AR, Pope SB, Goldin GM. A numerical study of auto-ignition in turbulent lifted flames issuing into a vitiated co-flow. Combust Theor Model 2007;11(3):351–76.
[58] Pope SB. PDF methods for turbulent reactive flows. Prog Energy Combust Sci 1985;11(2):119–92.
[59] Chen H, Chen S, Kraichnan RH. Probability distribution of a stochastically advected scalar field. Phys Rev Lett 1989;63(24):2657.
[60] Pope SB. Mapping closures for turbulent mixing and reaction. Theor Comput Fluid Dynam 1991;2(5):255–70.
[61] Sundaram B, Klimenko AY, Cleary MJ, Ge Y. A direct approach to generalised multiple mapping conditioning for selected turbulent diffusion flame cases. Combust Theor Model 2016;20(4):735–64.
[62] Lacaze G, Richardson E, Poinsot T. Large eddy simulation of spark ignition in a turbulent methane jet. Combust Flame 2009;156(10):1993–2009.
[63] Chassaing P. Turbulence en Mécanique des Fluides, Analyse du Phénomène en vue de sa Modélisation à L'usage de L'ingénieur, Cépaduès-éditions. Toulouse: France; 2000.
[64] Pope SB. Ten questions concerning the large-eddy simulation of turbulent flows. New J Phys 2004;6(1):35.

Please cite this article as: Li G et al., Large eddy simulation and finite-volume conditional moment closure modelling of a turbulent lifted H_2/N_2 flame, International Journal of Hydrogen Energy, https://doi.org/10.1016/j.ijhydene.2021.09.209